Applied Mathematical Modelling 118 (2023) 832–852

Contents lists available at ScienceDirect

Applied Mathematical Modelling

journal homepage: www.elsevier.com/locate/apm

Time-domain wave response of a compressible ocean due to an arbitrary ocean bottom motion

Santu Das[a,*], Michael H. Meylan[b]

[a] Mathematical and Computational Sciences (Physical Sciences Division), Institute of Advanced Study in Science and Technology, Guwahati 781035, India
[b] School of Information and Physical Sciences, University of Newcastle, NSW 2308, Australia

ARTICLE INFO

Article history:
Received 14 May 2022
Revised 10 January 2023
Accepted 20 January 2023
Available online 3 February 2023

Keywords:
Arbitrary motion of seafloor
Water compressibility
Surface wave profile
Fourier series expansion
Fourier transformation
Acoustic-gravity wave

ABSTRACT

The time-domain motion of a finite depth ocean subject to an arbitrary (in both time and space) imposed displacement of the bottom is studied under the assumption of linear theory. This solution provides results for this limiting case which may be helpful for benchmarking. The focus is on the numerical simulation of the near-field waves with application to the simulation of tsunami waves. The fluid domain is assumed two-dimensional, and the effect of compressibility is included. The time-domain solution is built from the frequency domain solution taking a Fourier series expansion of the bottom motion. This expansion allows complex displacements to be simulated. The solution in the frequency domain is expressed as a sum over modes. The time-domain solution is calculated by numerical evaluation of the Fourier transform in time, allowing arbitrary time-dependent motion. This code is extremely efficient and highly accurate, and there is no time–stepping so that errors do not accumulate in time. The eigenfunction expansion method to obtain the velocity potential for a flat ocean bottom case is independently derived. A shallow water limit for all the above cases is provided, giving a method to check the correctness of the numerical solution. Separate treatment for all the situations under the compressible assumption is also performed. The horizontal and vertical particle velocities are graphically presented for the time-harmonic oscillation. Time-dependent surface wave propagation is computed to show the initiation of tsunami waves in the deep ocean and their subsequent propagation. The calculations presented here allow for the simulation of tsunami wave generation and to investigate various effects, including the role of acoustic gravity waves. It is shown that the compressibility is not always significant, but that when the water is either sufficiently deep or the rise sufficiently rapid, acoustic gravity waves are produced. It is shown that, in this case, the ocean surface undergoes a rapid oscillation and that this may be a method to detect tsunamis.

1. Introduction

Coastal areas, including both land-mass and water, throughout the world have been the most significant part of human civilisation as more than 600 million people live in a coastal region within 10 m of elevation, which ac-

* Corresponding author.
E-mail addresses: d.santu@iasst.gov.in (S. Das), mike.meylan@newcastle.edu.au (M.H. Meylan).

https://doi.org/10.1016/j.apm.2023.01.030
0307-904X/

count for 10 per cent of the world population (https://www.un.org/sustainabledevelopment/wp-content/uploads/2017/05/Ocean-fact-sheet-package.pdf). On top of that, approximately 2.4 billion people, around 40 per cent of total world population, live within 100 kilometers of the coastline. Any threat to the coastal region thus possesses an enormous amount of potential damage to the world population, a country's economy, and natural food resources, to name a few. Among all the natural calamities, tsunamis possess a grave threat which is evident from the recent accounts of destruction caused by 2004 Indian Ocean, 2011 Tohoku Oki, 2018 Sulawesi and Palu tsunamis, which are caused following submarine earthquakes.

Predicting and simulating tsunami waves is of obvious importance in providing a reliable warning system. Detailed progress of tsunami research that includes state-of-the-art knowledge of the underlying physics, monitoring system, and mitigation mechanisms can be found in [1]. Numerical simulations play an essential role, and very sophisticated models have been developed [2]. In particular, the inclusion of compressibility allows for the simulation of acoustic gravity waves, which have been proposed as a method for early warning [3–5] although the method is in dispute [6]. However, it has also been shown that a tsunami model based on a compressible ocean is more accurate than a model with an incompressible ocean [4]. It is also essential to simulate different kinds of motions of the ocean bottom. An appropriate model taking the water compressibility into account and that can cater to such changes in the initial time-domain displacement is developed in this work.

Acoustic-gravity waves are low–frequency acoustic waves that propagate in the ocean analogous to modes in a waveguide. These waves are hydro-acoustic waves that are influenced by gravity at a low frequency. It is the mathematical treatment that differentiates acoustic-gravity waves from hydro-acoustic waves. These waves travel much faster than tsunami waves, but their generation depends on the properties of the ocean floor motion [3,5,7,8] and they have potential utility in detecting tsunamis. Under linear water wave theory, the compressibility alters some of the evanescent modes, the purely imaginary naturally occurring modes for the incompressible ocean, into real propagating modes. These newly generated waves are the acoustic-gravity waves that appear alongside the one purely gravity mode, in addition to the multiple propagating gravity modes, which may occur due to the exceptional case of wave blocking [9,10]. The oscillatory pressure signature generated at the ocean bottom as an outcome of the generation of acoustic-gravity waves can cause microseism [11]. These waves have the potential to cause deepwater transport [12], and even to impact on ice-sheets [13] as well as influence their breaking [14].

There are many other mechanisms, including the triad resonance (see [15–17]), horizontally moving wavemaker (see [18]), which generates acoustic-gravity waves. The triad resonance has been proposed to mitigate tsunami waves [19]. There are other complex contributing factors such as variable ocean bathymetry [20] causing reflection and scattering, surface gravity waves [21], and even by the dissipation caused by the bottom friction, elastic [22] and viscous [23] nature of the seafloor, and movement of marine sediment [24]. The effect of a porous ocean bottom is included in the mathematical formulation by Chierici et al. [25] in addition to the nonlinear temporal rise time of the fault. In all these factors, ocean water compressibility plays a pivotal role, which was pointed out through the fundamental works of [8,26,27]. Later, the idea was utilised and extended to the works of [4,5,28–30]. Earlier, [31] suggested the possible cause of tsunami time delay due to the effect of self-gravitating elastic earth. Later, [32] included the asymmetric earthquake motion into the formulation. On the other hand, [33] later included the gravity term in the governing equation and demonstrated its effect on both the acoustic-gravity and surface waves. The idea is further extended to include the influence of sea-floor elasticity [34,35]. Most of these works are based on acoustic-gravity waves generated by an elongated one-dimensional fault which was later extended to two dimensions by Hendin and Stiassnie [36] with the help of Green's function method. Further development occurred in terms of the mild-slope equation for these waves to tackle two-dimensional bathymetry and fault area [13,23,37]. These models apply to other generic bottom topography as long as the spatial variation is not so large. Very recently, the idea was extended to tackle the case of a slender fault [38] and later extended to multiple slender faults to emulate multi-fracture fault [39]. The geometry of all these faults has one aspect in common, i.e. the floor surface of the displacement is kept flat or slowly varying - be it one-dimensional or two-dimensional. Other types of ocean floor surfaces where the depth variation is large have not yet been attempted in any context.

This work studies the mathematical problem of surface wave propagation induced by a motion of the ocean bottom under the assumption of a compressible ocean. The mathematical problem is solved using the Fourier transformation technique, and the analytical form of the displacement potential function is obtained. Such methods have appeared previously in the literature, for example, [5,8,13] to name a few. These were limited to simple motions of the ocean bottom, and we extend this method to arbitrary motions using a Fourier series expansion for the bottom displacement. Moreover, the near field fluid motion was not simulated in previous works; only the asymptotic solution was derived. This is because the numerical expressions are complicated to work with. Moreover, no attempt was made to validate the method and neither was any computational code provided with the calculations. We validate our solution by showing it agrees with the simple shallow water solution in the limit of small depth. Moreover, the numerical solutions provided here are given as animations which elucidate the physics of the motion. We also note that the solution method provided is highly efficient and does not require any time stepping, and can serve as benchmark calculations.

Free surface elevation is evaluated numerically. A similar problem is solved using the rising ocean bottom instead of the oscillating bottom, making the mathematical problem time-dependent. The evolution of the surface profile over time under the influence of AGW is demonstrated along with its shallow water approximation and incompressible ocean case. Other forms of ocean bottoms are also approximated, including the flat bottom case. The influence of AGW is demonstrated with the help of a graphical representation of free surface elevation and the horizontal and vertical velocity distributions inside the water domain.

The paper is arranged in the following manner. The mathematical formulation of the physical problem of a compressible ocean is detailed in § 2 where the solution methodology for an arbitrary spatio-temporal displacement of the ocean floor is considered. The solution process for the single frequency involving the Fourier transform technique, which will be utilised to solve the problem described in § 2, is detailed in § 3. Different special cases involving flat ocean bottom, incompressible ocean, and shallow water approximation are considered in § 4. The graphical representations for the time-harmonic solution of flat ocean bottom case and time-dependent surface wave profile for two different choices of ocean bottom profiles are illustrated in § 5. The paper ends with a brief conclusion in § 6 followed by derivations of flat ocean bottom case using the eigenfunction expansion method and its incompressible shallow water counterpart.

2. Mathematical formulation

We consider free-surface gravity wave propagation in a compressible ocean of finite depth h. The inclusion of compressibility is essential to this work, and we will show that for typical tsunami wave cases, the inclusion of compressibility has a significant effect. Many other authors have shown this [4,26,29]. The physical problem is formulated in a two-dimensional Cartesian coordinate system having z- axis pointing upwards and x- axis horizontal. The ocean bed is characterised as rigid. A wave propagation due to the ocean floor disturbance is realised both towards the positive and negative x- direction under the assumption of linearised water wave theory. The flow is considered irrotational. We are interested in calculating the time-dependent motion of the fluid due to a movement of the seafloor, simulating the generation of a tsunami in two dimensions. We consider time dependent growth $l(t)$ of a fixed displacement function $\mathcal{X}(x)$ of the ocean bottom between $-b$ and b. We note that it would be straightforward to generalise to more complex motions which were not separable using linearity. Under these assumptions, the small amplitude displacement of the sea floor $\tilde{h}$ is given by,

$$\tilde{h}(x,t) = l(t)\mathcal{X}(x)\mathcal{H}(b^2 - x^2),$$

where $\mathcal{H}(\cdot)$ represents Heaviside unit step function. A few works such as [33] considered the density profile associated with the static compression of the ocean under its own weight. We here neglect such an effect mainly for two reasons. First, the majority of the literature does not include it. Secondly, we primarily focus on the solution methodology and the numerical calculation that can be used to validate other problems pertaining to an arbitrary spatio-temporal motion of the ocean bed. However, the inclusion of the ambient static compression is an interesting problem and can be taken as a future extension. Hence, the boundary value problem we wish to solve is given by

$$\nabla^2\Phi(x,z,t) = \frac{1}{c^2}\frac{\partial^2\Phi}{\partial t^2} \qquad \text{in} \quad -h < z < 0, \tag{1a}$$

$$\Phi_{tt} + g\Phi_z = 0 \qquad \text{at} \quad z = 0, \tag{1b}$$

$$\Phi_z = l(t)\mathcal{X}(x)\mathcal{H}(b^2 - x^2) \qquad \text{at} \quad z = -h. \tag{1c}$$

where Φ is the displacement potential, g is the acceleration due to gravity, $c = \dfrac{K_0}{\rho_0}$ is the speed of sound in water and K_0 being the bulk modulus, and ρ_0 is the undisturbed density of the whole water region. The gradient of Φ provides the water particle displacements along x (say u) and z (say v) directions, i.e., $\nabla\Phi = (u,\ v)$. Note that we are linearising about an infinitesimal motion so that the depth is assumed constant, precisely as is done at the free surface. We also assume that Φ and l are zero for $t < 0$, i.e., the fluid is initially at rest.

We use the linearisation in which the dimensional units are used here. The linear assumption is valid only for infinitesimal displacements. When we talk about the solution for $\tilde{h}$ we mean the solution for $\epsilon\tilde{h}$ for infinitesimal ϵ, which is then divided by ϵ. This point is often taken for granted and not mentioned explicitly. For example, it is not mentioned in [36]; however, it does underlie their (and our) solution.

We now return to our initial problem of a finite time growth of the ocean bottom between $-b$ and b. Applying a Fourier transformation in time (which is equivalent to a Laplace transform since the fluid is at rest),

$$\hat{\Phi}(x,z,\omega) = \int_0^\infty \Phi(x,z,t)e^{-\mathrm{i}\omega t}dt, \tag{2}$$

the boundary value problem (1) is converted to

$$\nabla^2\hat{\Phi}(x,z,\omega) = \frac{\omega^2}{c^2}\hat{\Phi}, \qquad \text{in} \quad -h < z < 0, \tag{3a}$$

$$\hat{\Phi}_z - \frac{\omega^2}{g}\hat{\Phi} = 0, \qquad \text{at} \quad z = 0, \tag{3b}$$

$$\hat{\Phi}_z = \mathcal{X}(x)\mathcal{H}(b^2 - x^2)\mathcal{W}(\omega), \qquad \text{at} \quad z = -h, \tag{3c}$$

where

$$\mathcal{W}(\omega) = \int_0^\infty l(t)e^{-\mathrm{i}\omega t}dt. \tag{4}$$

We write $\mathcal{X}(x)$ as a Fourier series

$$\mathcal{X}(x) = \left(\sum_{m=0}^{\infty} \zeta_c^m \cos\left(\frac{m\pi x}{b}\right) + \zeta_s^m \sin\left(\frac{m\pi x}{b}\right)\right) \tag{5}$$

We can find the solution as

$$\hat{\Phi}(x,z,\omega) = \mathcal{W}(\omega)\left(\sum_{m=0}^{\infty} \zeta_c^m \phi_c^m(x,z,\omega) + \zeta_s^m \phi_s^m(x,z,\omega)\right), \tag{6}$$

where ϕ_c^m and ϕ_s^m are the solutions of the boundary value problem for a single frequency for $\zeta_c^m = 1$ and all other terms zero or $\zeta_s^m = 1$ and all other terms zero respectively. They will be carefully defined and solved in the next section. Now taking the inverse Fourier transformation, we obtain the potential function as

$$\Phi(x,z,t) = \frac{1}{2\pi}\int_{-\infty}^{\infty} \hat{\Phi}(x,z,\omega)e^{\mathrm{i}\omega t}d\omega = \mathrm{Re}\left\{\frac{1}{\pi}\int_0^\infty \hat{\Phi}(x,z,\omega)e^{\mathrm{i}\omega t}d\omega\right\}. \tag{7}$$

3. Solution for a single frequency and sinusoidal bottom motion

We calculate the single frequency solution considering a complex exponential bottom profile from which we can extract the cosine and sine expansion (Fig. 1). We solve for the displacement potential ϕ^m which satisfies the following equations

$$\nabla^2\phi^m(x,z) = -\frac{\omega^2}{c^2}\phi^m \qquad \text{in} \quad -h < z < 0, \tag{8a}$$

$$-\omega^2\phi^m + g\phi_z^m = 0 \qquad \text{at} \quad z = 0, \tag{8b}$$

$$\phi_z^m = \exp\left(\mathrm{i}\frac{m\pi x}{b}\right)\mathcal{H}(b^2 - x^2) \qquad \text{at} \quad z = -h.\, m \in \mathbb{Z}. \tag{8c}$$

Notice that the boundary value problems defined in (3) and (8) are equivalent when $\mathcal{X}(x) = \exp\left(\mathrm{i}\frac{m\pi x}{b}\right)$ and $\mathcal{W}(\omega) = 1$. The real part of $\mathcal{X}(x)$ leads to the solution ϕ_c^m, where the imaginary part corresponds to ϕ_s^m. These computed values of ϕ_c^m and ϕ_s^m will be put into (6) to obtain the solution for arbitrary ocean bottom motion. It may also be noticed that the above boundary condition at the ocean bottom varies in the spatial coordinate but become simpler in wavenumber space. Thus a Fourier transformation in the wavenumber space is applied to solve the boundary value problem. This problem was solved in [8] for the $m = 0$ case. The solution here follows the method described in a similar fashion.

The problem will be solved by applying the Fourier transformation of the form

$$\mathcal{F}(k,z) = \int_{-\infty}^{\infty} \phi^m(x,z)\exp(-\mathrm{i}kx)dx, \tag{9}$$

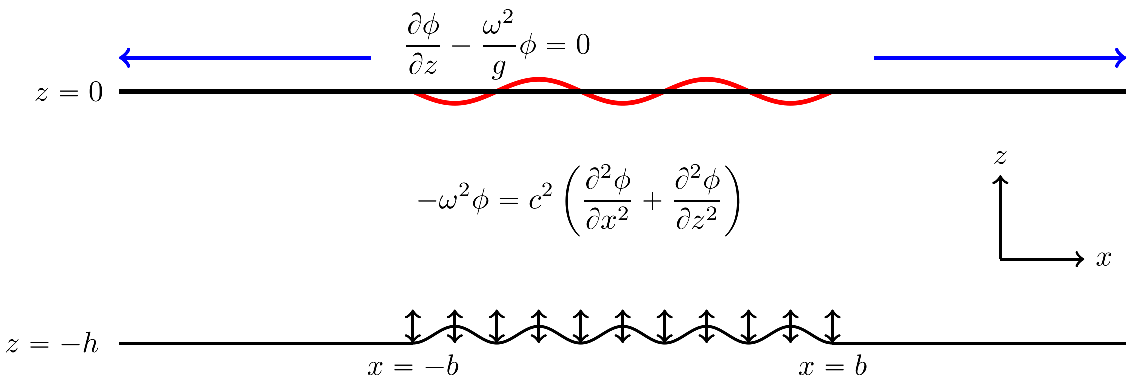

Fig. 1. Schematic diagram of the physical problem in a compressible ocean having sinusoidal ripple bottom.

whose inverse Fourier transformation is given by

$$\phi^m(x,z) = \frac{1}{2\pi}\int_{-\infty}^{\infty} \mathcal{F}(k,z)\exp(\mathrm{i}kx)dk, \tag{10}$$

and the set (8) transforms into the following boundary value problem:

$$\mathcal{F}_{zz} = \left(k^2 - \frac{\omega^2}{c^2}\right)\mathcal{F}, \qquad \text{in} \quad -h < z < 0, \tag{11a}$$

$$\mathcal{F}_z = \frac{\omega^2}{g}\mathcal{F}, \qquad \text{on} \quad z = 0, \tag{11b}$$

$$\mathcal{F}_z = \frac{2b\sin(m\pi - kb)}{m\pi - kb}, \qquad \text{on} \quad z = -h. \tag{11c}$$

Using separation of variables method, the solution to Eq. (11a) can be expressed as

$$\mathcal{F}(k,z) = A\cosh(\mu(z+h)) + B\sinh(\mu(z+h)) \quad \text{where} \quad \mu^2 = k^2 - \frac{\omega^2}{c^2}. \tag{12}$$

Applying the boundary conditions (11b) and (11c), the following pair of equations are obtained:

$$\left[\mu\sinh(\mu h) - \frac{\omega^2}{g}\cosh(\mu h)\right]A + \left[\mu\cosh(\mu h) - \frac{\omega^2}{g}\sinh(\mu h)\right]B = 0, \tag{13}$$

$$B = \frac{2\zeta_0 b\sin(m\pi - kb)}{\mu(m\pi - kb)}, \tag{14}$$

solving which we obtain

$$A = -\frac{2b\sin(m\pi - kb)\left[\mu\cosh\mu h - (\omega^2/g)\sinh\mu h\right]}{\mu(m\pi - kb)[\mu\sinh\mu h - (\omega^2/g)\cosh\mu h]}. \tag{15}$$

Thus the potential function $\mathcal{F}(k,z)$ can be expressed as

$$\mathcal{F}(k,z) = \frac{2(-1)^m b\sin(kb)}{\mu(m\pi - kb)\mathcal{D}(\mu,h)}\left[\mu\cosh\mu z + \frac{\omega^2}{g}\sinh\mu z\right], \tag{16}$$

where

$$\mathcal{D}(\mu,h) = \mu\sinh(\mu h) - \frac{\omega^2}{g}\cosh(\mu h). \tag{17}$$

Taking the inverse Fourier transform, the velocity potential $\phi^m(x,z)$ is obtained as

$$\phi^m(x,z) = \frac{(-1)^m b}{\pi}\int_{-\infty}^{\infty}\frac{\sin kb\left[\mu\cosh\mu z + (\omega^2/g)\sinh\mu z\right]}{\mu(m\pi - kb)\mathcal{D}(\mu,h)}e^{\mathrm{i}kx}dk, \tag{18a}$$

$$= \frac{(-1)^m b}{2\pi\mathrm{i}}\int_{-\infty}^{\infty} M(k,z)\left[e^{\mathrm{i}k(x+b)} - e^{\mathrm{i}k(x-b)}\right]dk, \tag{18b}$$

where

$$M(k,z) = \frac{\mu\cosh\mu z + (\omega^2/g)\sinh\mu z}{\mu(m\pi - kb)\mathcal{D}(\mu,h)} \tag{19}$$

It will be easier to evaluate the above integral when we consider another integral of the form

$$\mathbb{F}(\xi,z) = \int_{-\infty}^{\infty} M(k,z)e^{\mathrm{i}k\xi}dk, \tag{20}$$

and write

$$\phi^m(x,z) = \frac{b(-1)^m}{2\pi\mathrm{i}}(\mathbb{F}(x+b,z) - \mathbb{F}(x-b,z)). \tag{21}$$

$M(k,z)$ has singularities at the following points:

$$k = \frac{m\pi}{b}, \quad \mu = 0 \quad \text{and} \quad \mu\sinh(\mu h) - \frac{\omega^2}{g}\cosh(\mu h) = 0. \tag{22}$$

The singularity at $k = \frac{m\pi}{b}$ is a removable one and will use the form

$$\lim_{\epsilon \to 0} \left(\frac{m\pi}{b} + \mathrm{i}\epsilon \right) = \frac{m\pi}{b}$$

to calculate the integral. We may choose the other form $\left(\frac{m\pi}{b} - \mathrm{i}\epsilon\right)$, but it will not affect the form of the potential function to be obtained using (21). The last equation of (22) is the dispersion relation for surface-gravity waves, and the solution is given by

$$\mu = \pm\mu_0, \quad \text{and} \quad \mu = \pm\mathrm{i}\mu_n \; (n = 1, 2, \dots), \tag{23}$$

where μ_0 and μ_n generate propagating and evanescent modes, respectively, and the roots are located at the points

$$k = \left(\frac{m\pi}{b} + \mathrm{i}\epsilon \right), \; \pm\frac{\omega}{c}, \; \pm k_0, \; \pm k_n, \; \pm\mathrm{i}\lambda_n \; (n = 1, 2, \dots),$$

where k_0, ka_n, λ_n are positive real numbers, and expressed as

$$k_0 = \sqrt{\mu_0^2 + \frac{\omega^2}{c^2}}, \tag{24a}$$

$$k_n = \sqrt{\frac{\omega^2}{c^2} - \mu_n^2}, \quad \left(\frac{\omega}{c} > \mu_n \right), \tag{24b}$$

$$\lambda_n = \sqrt{\mu_n^2 - \frac{\omega^2}{c^2}}, \quad \left(\frac{\omega}{c} < \mu_n \right). \tag{24c}$$

Here $\frac{\omega}{c}$ represents the wavenumber of sound wave in water, k_0 is propagating purely surface-gravity mode (larger wavenumber compared to μ_0 of an incompressible fluid), λ_n are attenuation coefficients of evanescent modes in compressible ocean and are smaller than μ_n - the attenuation coefficient of evanescent modes for an incompressible fluid. The evanescent modes μ_n for incompressible fluid are converted to propagating acoustic-gravity modes (with wavenumber k_n) in compressible ocean once the wavenumber of sound wave becomes larger than μ_n. The mode $k_e = m\pi/b$ is due to the ripples in the elevated bed, and we assume this wave mode not to be overlapping with any other wave modes.

The wave periodicity is proportional to $e^{\mathrm{i}\omega t}$. The contours for $\xi > 0$ and $\xi < 0$ are given in Fig. 2.

While Fig. 2(a) shows the contour for waves propagating in the positive direction, Fig. 2(b) shows the same for negative direction.

We will apply the above contour scheme to find the integral given in (20). First, we distribute the spatial length into the following 3 parts.

$$(i) \; -\infty < x < -b, \quad (ii) \; -b < x < b \quad \text{and} \quad (iii) \; b < x < \infty. \tag{25}$$

The following three contour schemes will be applied to these three regions.

(i) $-\infty < x < -b$: Here, the contour taken will be such that all the waves corresponding to $\mathbb{F}(x \pm b)$ travel towards the negative direction. Hence, we take the contour given in the first subplot of Fig. 2(b), which we will refer to as a TYPE-b$^-$ contour.

(ii) $b < x < \infty$: Here, the contour taken will be such that all the waves corresponding to $\mathbb{F}(x \pm b)$ travel towards the positive direction. Hence, we take the contour given in the first subplot of Fig. 2(a), which we refer to TYPE-a$^+$.

(iii) $-b < x < b$: Here, the contribution due to $\mathbb{F}(x + b)$ will be those waves travelling towards the positive direction. Thus the appropriate contour will be the TYPE-a$^+$. The same from $\mathbb{F}(x - b)$ will be the waves travelling in the negative direction. Thus the corresponding contour will be the TYPE-b$^-$.

Now we shift our focus to the contour integration. The evaluation of the integrals is based on the calculation of residue at the points of singularities of the function $M(k, z)$. For $x > b$, we obtain $x \pm b > 0$. Hence, the contour for $\xi > 0$ will be applicable for both $\mathbb{F}(x \pm b, z)$ (Fig. 3). Consequently,

$$\mathbb{F}(x \pm b, z) = 2\pi\mathrm{i} \left[\sum_{n=1}^{\infty} \mathrm{Res}(x \pm b, \mathrm{i}\lambda_n) + \mathrm{Res}(x \pm b, -k_0) + \mathrm{Res}(x \pm b, -k_s) + \sum_{n=1}^{N} \mathrm{Res}(x \pm b, -k_n) \right].$$

For $x < -b$, we obtain $x \pm b < 0$. Hence, the contour for $\xi < 0$ will be applicable for both $\mathbb{F}(x \pm b, z)$ (Fig. 3). Consequently,

$$\begin{aligned} \mathbb{F}(x \pm b, z) = &- 2\pi\mathrm{i} \left[\sum_{n=1}^{\infty} \mathrm{Res}(x \pm b, -\mathrm{i}\lambda_n) + \mathrm{Res}(x \pm b, k_0) + \mathrm{Res}(x \pm b, k_s) + \sum_{n=1}^{N} \mathrm{Res}(x \pm b, k_n) \right] \\ &- \lim_{\epsilon \to 0} 2\pi\mathrm{i}\,\mathrm{Res}(x \pm b, m\pi/b + \mathrm{i}\epsilon). \end{aligned}$$

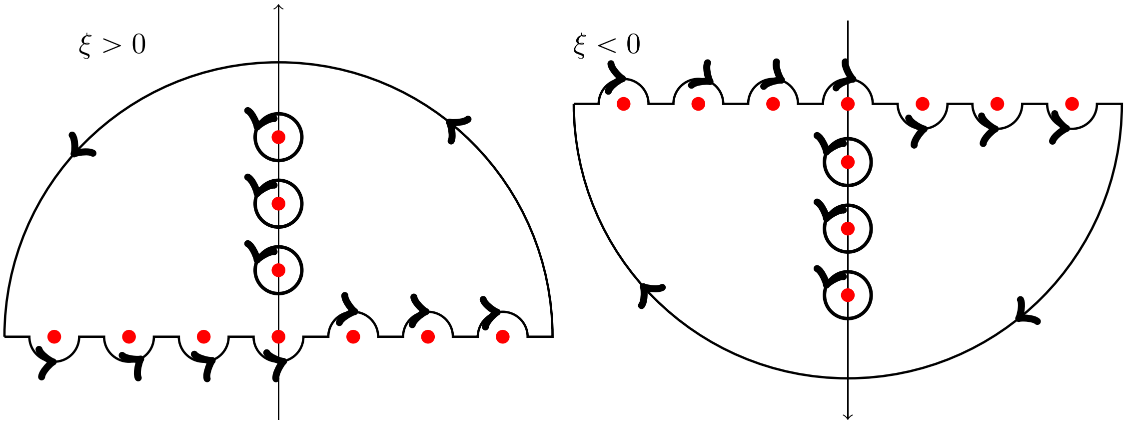

(a) For waves propagating in the positive direction

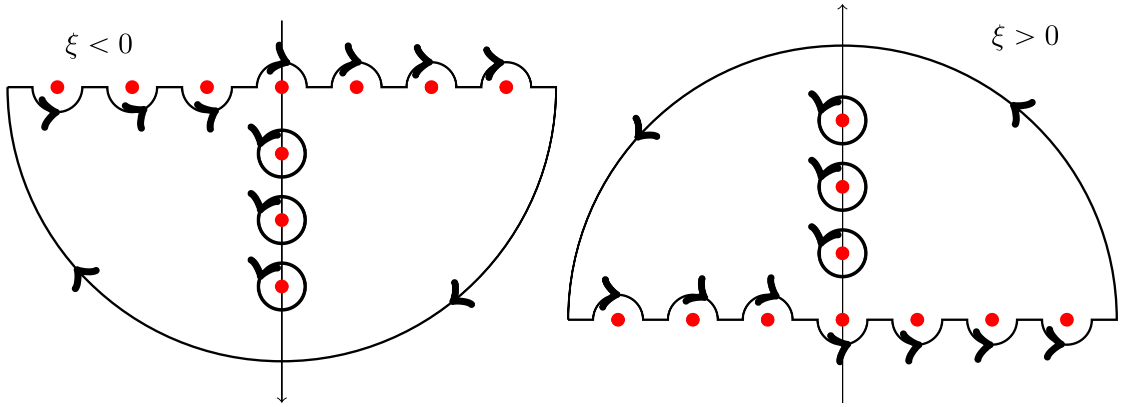

(b) For waves propagating in the negative direction

Fig. 2. Contours for the integral of the form given in Eq. (20).

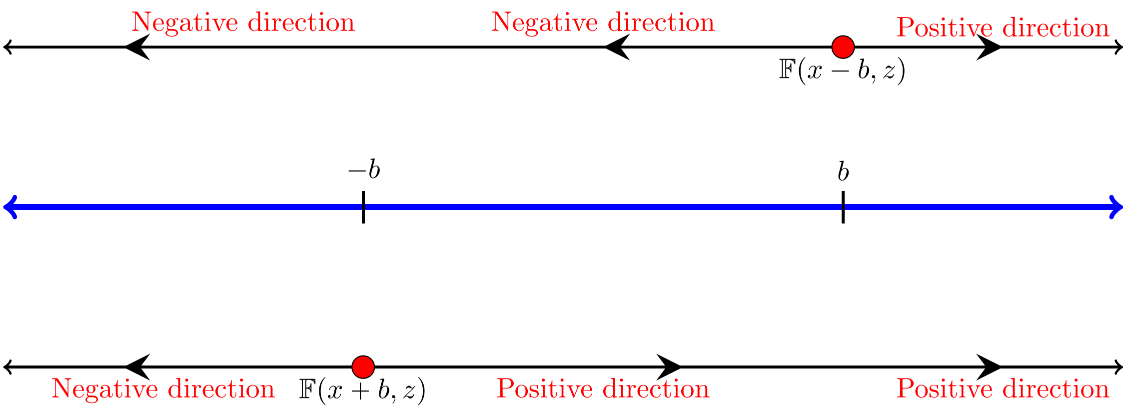

Fig. 3. Schematic diagram showing the wave directions due to the functions $\mathbb{F}(x \pm b)$ in different spatial regions.

For $-b < x < b$, we obtain $x + b > 0$ and $x - b < 0$. Hence, the contour for $\xi < 0$ will be applicable for $\mathbb{F}(x - b, z)$, and $\mathbb{F}(x + b, z)$ will use the contour for $\xi > 0$ (Fig. 3). Consequently,

$$\mathbb{F}(x + b, z) = 2\pi \mathrm{i}\left[\sum_{n=1}^{\infty} \mathrm{Res}(x + b, \mathrm{i}\lambda_n) + \mathrm{Res}(x + b, -k_0) + \mathrm{Res}(x + b, -k_s) + \sum_{n=1}^{N} \mathrm{Res}(x + b, -k_n)\right].$$

$$\mathbb{F}(x-b,z) = -2\pi\mathrm{i}\left[\sum_{n=1}^{\infty}\mathrm{Res}(x-b,-\mathrm{i}\lambda_n)+\mathrm{Res}(x-b,k_0)+\mathrm{Res}(x-b,k_s)+\sum_{n=1}^{N}\mathrm{Res}(x-b,k_n)\right] - \lim_{\epsilon\to 0} 2\mathrm{i}\,\mathrm{Res}(x-b,m\pi/b+\mathrm{i}\epsilon).$$

Now putting the above expressions of $\mathbb{F}(x\pm b)$, region-wise, back into (21),

$$\phi^m(x,z) = \begin{cases} \Bigg[\sum_{n=1}^{\infty}\{\mathrm{Res}(x+b,\mathrm{i}\lambda_n)-\mathrm{Res}(x-b,\mathrm{i}\lambda_n)\}+\{\mathrm{Res}(x+b,-k_0)-\mathrm{Res}(x-b,-k_0)\} \\ \quad +\sum_{n=1}^{N}\{\mathrm{Res}(x+b,-k_n)-\mathrm{Res}(x-b,-k_n)\}+\{\mathrm{Res}(x+b,-k_s)-\mathrm{Res}(x-b,-k_s)\}\Bigg] \\ \quad \times b(-1)^m \qquad \text{if } x>b, \\ -\Bigg[\sum_{n=1}^{\infty}\{\mathrm{Res}(x+b,-\mathrm{i}\lambda_n)-\mathrm{Res}(x-b,-\mathrm{i}\lambda_n)\}+\{\mathrm{Res}(x+b,k_0)-\mathrm{Res}(x-b,k_0)\} \\ \quad +\sum_{n=1}^{N}\{\mathrm{Res}(x+b,k_n)-\mathrm{Res}(x-b,k_n)\}+\{\mathrm{Res}(x+b,k_s)-\mathrm{Res}(x-b,k_s)\} \\ \quad +\lim_{\epsilon\to 0}\left\{\mathrm{Res}\left(x+b,\frac{m\pi}{b}+\mathrm{i}\epsilon\right)-\mathrm{Res}\left(x-b,\frac{m\pi}{b}+\mathrm{i}\epsilon\right)\right\}\Bigg]b(-1)^m \qquad \text{if } x<-b, \\ \Bigg[\sum_{n=1}^{\infty}\{\mathrm{Res}(x+b,\mathrm{i}\lambda_n)+\mathrm{Res}(x-b,-\mathrm{i}\lambda_n)\}+\mathrm{Res}(x+b,-k_0)+\mathrm{Res}(x-b,k_0) \\ \quad +\sum_{n=1}^{N}\{\mathrm{Res}(x+b,-k_n)+\mathrm{Res}(x-b,k_n)\}+\{\mathrm{Res}(x+b,-k_s)+\mathrm{Res}(x-b,k_s)\} \\ \quad +\lim_{\epsilon\to 0}\mathrm{Res}\left(x-b,\frac{m\pi}{b}+\mathrm{i}\epsilon\right)\Bigg]b(-1)^m \qquad \text{if } -b<x<b \end{cases}.$$

Note that the potential function $\phi(x,z)$ is a function of ω as well and we denote it by $\phi(x,z,\omega)$ from now onward. The residues are calculated to be

$$\mathrm{Res}(x,\pm k_0) = \pm\frac{2\mu_0\cosh\mu_0(z+h)}{k_0(m\pi\mp k_0b)(2\mu_0h+\sinh 2\mu_0h)}e^{\pm\mathrm{i}k_0x}, \tag{26a}$$

$$\mathrm{Res}\left(x,\pm\frac{\omega}{c}\right) = 0, \tag{26b}$$

$$\mathrm{Res}\left(x,\left(\frac{m\pi}{b}+\mathrm{i}\epsilon\right)\right) = -\frac{\mu_e\cosh\mu_ez+\frac{\omega^2}{g}\sinh\mu_ez}{\mu_eb\mathcal{D}(\mu_e,h)}\exp\left(\pm\mathrm{i}\left(\frac{m\pi}{b}+\mathrm{i}\epsilon\right)x\right) \quad \text{where} \quad \mu_e=\sqrt{\left(\frac{m\pi}{b}+\mathrm{i}\epsilon\right)^2-\frac{\omega^2}{c^2}}, \tag{26c}$$

$$\mathrm{Res}(x,\pm k_n) = \pm\frac{2\mu_n\cos\mu_n(z+h)}{k_n(m\pi\mp k_nb)(2\mu_nh+\sin 2\mu_nh)}e^{\pm\mathrm{i}k_nx} \qquad n=1,2,\ldots,N, \tag{26d}$$

$$\mathrm{Res}(x,\pm\mathrm{i}\lambda_n) = \pm\frac{2\mu_n\cos\mu_n(z+h)}{\lambda_n(\mathrm{i}m\pi\pm\lambda_nb)(2\mu_nh+\sin 2\mu_nh)}e^{\mp\lambda_nx} \qquad n=N+1,\ldots. \tag{26e}$$

It is easy to verify that

$$\lim_{\epsilon\to 0}\left\{\mathrm{Res}\left(x+b,\frac{m\pi}{b}+\mathrm{i}\epsilon\right)-\mathrm{Res}\left(x-b,\frac{m\pi}{b}+\mathrm{i}\epsilon\right)\right\} = \left[\frac{\mu_e\cosh\mu_ez+(\omega^2/g)\sinh\mu_ez}{\mu_eb\mathcal{D}(\mu_e,h)}\right]e^{\mathrm{i}k_ex}2\mathrm{i}\sin(m\pi)=0.$$

Now the potential function is retrieved as

$$\phi^m(x,z,\omega)|_{|x|>b} = \pm b(-1)^m\Bigg\{\frac{4\mathrm{i}\mu_0\cosh(\mu_0(z+h))\sin(k_0b)e^{\mp\mathrm{i}k_0x}}{k_0(m\pi\pm k_0b)(2\mu_0h+\sinh 2\mu_0h)} + \sum_{n=1}^{N}\frac{4\mathrm{i}\mu_n\cos(\mu_n(z+h))\sin(k_nb)e^{\mp\mathrm{i}k_nx}}{k_n(m\pi\pm k_nb)(2\mu_nh+\sin 2\mu_nh)} - \sum_{n=N+1}^{\infty}\frac{4\mu_n\sinh(\lambda_nb)\cos\mu_n(z+h)e^{\mp\lambda_nx}}{\lambda_n(\mathrm{i}m\pi\pm\lambda_nb)(2\mu_nh+\sin 2\mu_nh)}\Bigg\}. \tag{27}$$

where the + sign is for $x > b$ and - sign is for $x < -b$. The above equation can be written in the following form by equating $\mathrm{i}k_n = \lambda_n$ etc.

$$\phi^m(x,z,\omega)|_{|x|>b} = \mp b(-1)^m \sum_{n=0}^{\infty} \frac{4\mu_n \sinh(\lambda_n b)\cos\mu_n(z+h)e^{\mp\lambda_n x}}{\lambda_n(\mathrm{i}m\pi \pm \lambda_n b)(2\mu_n h + \sin 2\mu_n h)}. \tag{28}$$

This form is ideal for computation. However, we stick to the form (27) so that the clear distinction among pure gravity, acoustic-gravity and evanescent modes are visible. This matches with the derivation of [8] for the $m = 0$ case. We also provide a separate derivation for the $m = 0$ case for incompressible fluid in Appendix A.

The upper sign is for $x > b$, and the lower sign is for $x < -b$. When $|x| < b$, the following form of $\phi(x,z,\omega)$ is obtained:

$$\begin{aligned}\phi^m(x,z,\omega)|_{|x|<b} = b(-1)^m \Bigg\{ & \frac{4\mu_0 \cosh\mu_0(z+h)e^{-\mathrm{i}k_0 b}(m\pi\,\mathrm{i}\sin(k_0x) + k_0 b\cos(k_0 x))}{k_0(m^2\pi^2 - k_0^2 b^2)(2\mu_0 h + \sinh 2\mu_0 h)} \\ & + \sum_{n=1}^{N} \frac{4\mu_n \cos\mu_n(z+h)e^{-\mathrm{i}k_n b}(m\pi\,\mathrm{i}\sin(k_n x) + k_n b\cos(k_n x))}{k_n(m^2\pi^2 - k_n^2 b^2)(2\mu_n h + \sin 2\mu_n h)} \\ & + \sum_{n=N+1}^{\infty} \frac{4\mu_n e^{-\lambda_n b}\cos(\mu_n(z+h))(\mathrm{i}m\pi\,\sinh(\lambda_n x) + \lambda_n b\cosh(\lambda_n x))}{\lambda_n(m^2\pi^2 + \lambda_n^2 b^2)(2\mu_n h + \sin(2\mu_n h))} \Bigg\} \\ & - (-1)^m \frac{\xi_m \cosh\xi_m z + (\omega^2/g)\sinh\xi_m z}{\xi_m \mathcal{D}(\xi_m, h)} e^{\mathrm{i}m\pi(x+b)/b}, \text{ where } \xi_m = \sqrt{\frac{m^2\pi^2}{b^2} - \frac{\omega^2}{c^2}}.\end{aligned} \tag{29}$$

The solution for cosine type bottom $(\cos(m\pi x/b))$ can be retrieved as

$$\phi_c^m(x,z,\omega) = \frac{\phi^m(x,z,\omega) + \phi^{-m}(x,z,\omega)}{2}.$$

The region-wise explicit forms for the potential function turn out to be

$$\begin{aligned}\phi_c^m(x,z,\ \omega)|_{|x|>b} = b^2(-1)^m \Bigg\{ & \frac{-4\mathrm{i}\mu_0 \sin(k_0 b)\cosh(\mu_0(z+h))e^{\mp\mathrm{i}k_0 x}}{(m^2\pi^2 - k_0^2 b^2)(2\mu_0 h + \sinh(2\mu_0 h))} \\ & + \sum_{n=1}^{N} \frac{-4\mathrm{i}\mu_n \sin(k_n b)\cos(\mu_n(z+h))e^{\mp\mathrm{i}k_n x}}{(m^2\pi^2 - k_n^2 b^2)(2\mu_n h + \sin(2\mu_n h))} - \sum_{n=N+1}^{\infty} \frac{4\mu_n \sinh(\lambda_n b)\cos(\mu_n(z+h))e^{\mp\lambda_n x}}{(m^2\pi^2 + \lambda_n^2 b^2)(2\mu_n h + \sin(2\mu_n h))} \Bigg\}\end{aligned} \tag{30}$$

The upper sign is for $x > b$, and the lower sign is for $x < -b$. When $|x| < b$, the following form of $\phi_c^m(x,z,\omega)$ is obtained:

$$\begin{aligned}\phi_c^m(x,z,\omega)|_{|x|<b} = b^2(-1)^m \Bigg\{ & \frac{4\mu_0 \cosh(\mu_0(z+h))e^{-\mathrm{i}k_0 b}\cos(k_0 x)}{(m^2\pi^2 - k_0^2 b^2)(2\mu_0 h + \sinh(2\mu_0 h))} \\ & + \sum_{n=1}^{N} \frac{4\mu_n \cos(\mu_n(z+h))e^{-\mathrm{i}k_n b}\cos(k_n x)}{(m^2\pi^2 - k_n^2 b^2)(2\mu_n h + \sin(2\mu_n h))} + \sum_{n=N+1}^{\infty} \frac{4\mu_n e^{-\lambda_n b}\cos(\mu_n(z+h))\cosh(\lambda_n x)}{(m^2\pi^2 + \lambda_n^2 b^2)(2\mu_n h + \sin(2\mu_n h))} \Bigg\} \\ & - \frac{\xi_m \cosh\xi_m z + \frac{\omega^2}{g}\sinh\xi_m z}{\xi_m\left(\xi_m \sinh(\xi_m h) - \frac{\omega^2}{g}\cosh(\xi_m h)\right)} \cos\left(\frac{m\pi x}{b}\right), \quad \text{where} \quad \xi_m = \sqrt{\frac{m^2\pi^2}{b^2} - \frac{\omega^2}{c^2}}.\end{aligned} \tag{31}$$

Similarly, the same results for the sine type bottom $(\sin(m\pi x/b))$ can be obtained as

$$\phi_s^m(x,z,\omega) = \frac{\phi^m(x,z,\omega) - \phi^{-m}(x,z,\omega)}{2\mathrm{i}}.$$

The potential function in the region $|x| > b$ is calculated to be

$$\begin{aligned}\phi_s^m(x,z,\omega)|_{|x|>b} = \pm(-1)^m bm\pi \Bigg\{ & \frac{4\mu_0 \sin(k_0 b)\cosh(\mu_0(z+h))e^{\mp\mathrm{i}k_0 x}}{k_0(m^2\pi^2 - k_0^2 b^2)(2\mu_0 h + \sinh(2\mu_0 h))} \\ & + \sum_{n=1}^{N} \frac{4\mu_n \sin(k_n b)\cos(\mu_n(z+h))e^{\mp\mathrm{i}k_n x}}{k_n(m^2\pi^2 - k_n^2 b^2)(2\mu_n h + \sin(2\mu_n h))} + \sum_{n=N+1}^{\infty} \frac{4\mu_n \sinh(\lambda_n b)\cos(\mu_n(z+h))e^{\mp\lambda_n x}}{\lambda_n(m^2\pi^2 + \lambda_n^2 b^2)(2\mu_n h + \sin(2\mu_n h))} \Bigg\},\end{aligned} \tag{32}$$

and the same in the region $|x| < b$ is found to be

$$\phi_s^m(x,z,\omega)|_{|x|<b} = (-1)^m bm\pi \left\{ \frac{4\mu_0 \cosh(\mu_0(z+h))e^{-\mathrm{i}k_0 b}\sin(k_0 x)}{k_0(m^2\pi^2 - k_0^2 b^2)(2\mu_0 h + \sinh(2\mu_0 h))} + \sum_{n=1}^{N} \frac{4\mu_n \cos(\mu_n(z+h))e^{-\mathrm{i}k_n b}\sin(k_n x)}{k_n(m^2\pi^2 - k_n^2 b^2)(2\mu_n h + \sin(2\mu_n h))} + \sum_{n=N+1}^{\infty} \frac{4\mu_n \cos(\mu_n(z+h))e^{-\lambda_n b}\sinh(\lambda_n x)}{\lambda_n(m^2\pi^2 + \lambda_n^2 b^2)(2\mu_n h + \sin(2\mu_n h))} \right\} - \frac{\left(\xi_m \cosh \xi_m z + \frac{\omega^2}{g}\sinh \xi_m z\right)}{\xi_m\left(\xi_m \sinh(\xi_m h) - \frac{\omega^2}{g}\cosh(\xi_m h)\right)} \sin\left(\frac{m\pi x}{b}\right). \tag{33}$$

The conventions for the upper and lower signs remain the same as before. Let us define the following quantities

$$f^m(x,\omega) = \left.\frac{\partial \phi^m(x,z,\omega)}{\partial z}\right|_{z=0}, \quad f_c^m(x,\omega) = \left.\frac{\partial \phi_c^m(x,z,\omega)}{\partial z}\right|_{z=0} \quad \text{and} \quad f_s^m(x,\omega) = \left.\frac{\partial \phi_s^m(x,z,\omega)}{\partial z}\right|_{z=0},$$

which will be required to calculate the surface elevation at a later stage.

4. Special cases

We present a few special case formulas that follow our derivation and which we use for the numerical calculations.

4.1. Surface elevation

The free surface displacement is written as

$$\eta(x,t) = \left.\frac{\partial \Phi}{\partial z}\right|_{z=0}.$$

We present here a formula for the surface elevation, which is

$$\eta(x,t) = \frac{1}{\pi}\sum_{m=0}^{\infty} \zeta_m^c \mathrm{Re}\left\{\int_0^\infty \mathcal{W}(\omega,\tau) f_c^m(x,\omega)e^{\mathrm{i}\omega t}d\omega\right\} + \frac{1}{\pi}\sum_{m=1}^{\infty} \zeta_s^m \mathrm{Re}\left\{\int_0^\infty \mathcal{W}(\omega,\tau) f_s^m(x,\omega)e^{\mathrm{i}\omega t}d\omega\right\}. \tag{34}$$

Note that this expression for $m = 0$ is closely related to that given in [5] except that we keep the rise time general here. Note that no numerical calculations of this expression were given there.

The first integral in the RHS represents the surface elevation when $\cos(m\pi x/b)$ type bottom is considered, and the second term represents the same for $\sin(m\pi x/b)$ type bottom.

The region-wise $f_c^m(x,\omega)$ is given by

$$f_c^m(x,\omega)|_{|x|>b} = b^2(-1)^m \left\{ \frac{-4\mathrm{i}\mu_0^2 \sin(k_0 b)\sinh(\mu_0 h)e^{\mp \mathrm{i}k_0 x}}{(m^2\pi^2 - k_0^2 b^2)(2\mu_0 h + \sinh(2\mu_0 h))} + \sum_{n=1}^{N} \frac{4\mathrm{i}\mu_n^2 \sin(k_n b)\sin(\mu_n h)e^{\mp \mathrm{i}k_n x}}{(m^2\pi^2 - k_n^2 b^2)(2\mu_n h + \sin(2\mu_n h))} + \sum_{n=N+1}^{\infty} \frac{4\mu_n^2 \sinh(\lambda_n b)\sin(\mu_n h)e^{\mp\lambda_n x}}{(m^2\pi^2 + \lambda_n^2 b^2)(2\mu_n h + \sin(2\mu_n h))} \right\}, \tag{35a}$$

$$f_c^m(x,\omega)|_{|x|<b} = b^2(-1)^m \left\{ \frac{4\mu_0^2 \sinh(\mu_0 h)e^{-\mathrm{i}k_0 b}\cos(k_0 x)}{(m^2\pi^2 - k_0^2 b^2)(2\mu_0 h + \sinh(2\mu_0 h))} - \sum_{n=1}^{N} \frac{4\mu_n^2 \sin(\mu_n h)e^{-\mathrm{i}k_n b}\cos(k_n x)}{(m^2\pi^2 - k_n^2 b^2)(2\mu_n h + \sin(2\mu_n h))} - \sum_{n=N+1}^{\infty} \frac{4\mu_n^2 e^{-\lambda_n b}\sin(\mu_n h)\cosh(\lambda_n x)}{(m^2\pi^2 + \lambda_n^2 b^2)(2\mu_n h + \sin(2\mu_n h))} \right\} - \zeta_0 \frac{\frac{\omega^2}{g}}{\xi_m \sinh(\xi_m h) - \frac{\omega^2}{g}\cosh(\xi_m h)} \cos\left(\frac{m\pi x}{b}\right). \tag{35b}$$

Note that when $m = 0$, this reduces to that given by [8]. The same for $f_s^m(x,\omega)$ are obtained as

$$f_m^s(x,\omega)|_{|x|>b} = \pm(-1)^m bm\pi \left\{ \frac{4\mu_0^2 \sin(k_0 b)\sinh(\mu_0 h)e^{\mp \mathrm{i}k_0 x}}{k_0(m^2\pi^2 - k_0^2 b^2)(2\mu_0 h + \sinh(2\mu_0 h))} - \sum_{n=1}^{N} \frac{4\mu_n^2 \sin(k_n b)\sin(\mu_n h)e^{\mp \mathrm{i}k_n x}}{k_n(m^2\pi^2 - k_n^2 b^2)(2\mu_n h + \sin(2\mu_n h))} - \sum_{n=N+1}^{\infty} \frac{4\mu_n^2 \sinh(\lambda_n b)\sin(\mu_n h)e^{\mp\lambda_n x}}{\lambda_n(m^2\pi^2 + \lambda_n^2 b^2)(2\mu_n h + \sin(2\mu_n h))} \right\}, \tag{36a}$$

$$f_m^s(x,\omega)|_{|x|<b} = (-1)^m bm\pi \left\{ \frac{4\mu_0^2 \sinh(\mu_0 h) e^{-\mathrm{i}k_0 b} \sin(k_0 x)}{k_0(m^2\pi^2 - k_0^2 b^2)(2\mu_0 h + \sinh(2\mu_0 h))} - \sum_{n=1}^{N} \frac{4\mu_n^2 \sin(\mu_n h) e^{-\mathrm{i}k_n b} \sin(k_n x)}{k_n(m^2\pi^2 - k_n^2 b^2)(2\mu_n h + \sin(2\mu_n h))} - \sum_{n=N+1}^{\infty} \frac{4\mu_n^2 \sin(\mu_n h) e^{-\lambda_n b} \sinh(\lambda_n x)}{\lambda_n(m^2\pi^2 + \lambda_n^2 b^2)(2\mu_n h + \sin(2\mu_n h))} \right\} - \frac{\frac{\omega^2}{g}}{\xi_m \sinh(\xi_m h) - \frac{\omega^2}{g}\cosh(\xi_m h)} \sin\left(\frac{m\pi x}{b}\right). \tag{36b}$$

4.2. Incompressible ocean with different types of ocean bottom

In the case of incompressible ocean, the AGW modes disappear, i.e., k_n $(n = 1, 2, \dots, N)$ vanishes, and $\mu_0 = k_0$, $\mu_n = \lambda_n$. All the cases considered for a compressible ocean, i.e., sine, cosine and flat ocean bottom with shallow water approximation, and the cases of the time-dependent rise of the fault could be obtained using the approximation $\omega/c = k_s = 0$ in the results obtained for the compressible case.

4.3. Flat oscillating ocean bottom

This case can be approximated by putting $m = 0$ in the cosine type bottom, and the region-wise displacement potential function can be written from Eqs. (30) and (31). The horizontal displacement component can be written as

$$\left.\frac{\partial\phi^0}{\partial x}\right|_{|x|>b} = \pm\left\{ \frac{4\mu_0 \sin(k_0 b)\cosh(\mu_0(z+h)) e^{\mp \mathrm{i}k_0 x}}{k_0(2\mu_0 h + \sinh(2\mu_0 h))} + \sum_{n=1}^{N} \frac{4\mu_n \sin(k_n b)\cos(\mu_n(z+h)) e^{\mp \mathrm{i}k_n x}}{k_n(2\mu_n h + \sin(2\mu_n h))} + \sum_{n=N+1}^{\infty} \frac{4\mu_n \sinh(\lambda_n b)\cos(\mu_n(z+h)) e^{\mp\lambda_n x}}{\lambda_n(2\mu_n h + \sin(2\mu_n h))} \right\}, \tag{37a}$$

$$\left.\frac{\partial\phi^0}{\partial x}\right|_{|x|<b} = \frac{4\mu_0 \cosh(\mu_0(z+h)) e^{-\mathrm{i}k_0 b}\sin(k_0 x)}{k_0(2\mu_0 h + \sinh(2\mu_0 h))} + \sum_{n=1}^{N} \frac{4\mu_n \cos(\mu_n(z+h)) e^{-\mathrm{i}k_n b}\sin(k_n x)}{k_n(2\mu_n h + \sin(2\mu_n h))} + \sum_{n=N+1}^{\infty} \frac{4\mu_n e^{-\lambda_n b}\cos(\mu_n(z+h))\sinh(\lambda_n x)}{\lambda_n(2\mu_n h + \sin(2\mu_n h))}. \tag{37b}$$

Similarly, the vertical displacement components are written as

$$\left.\frac{\partial\phi^0}{\partial z}\right|_{|x|>b} = \frac{4\mathrm{i}\mu_0^2 \sin(k_0 b)\sinh(\mu_0(z+h)) e^{\mp \mathrm{i}k_0 x}}{k_0^2(2\mu_0 h + \sinh(2\mu_0 h))} - \sum_{n=1}^{N} \frac{4\mathrm{i}\mu_n^2 \sin(k_n b)\sin(\mu_n(z+h)) e^{\mp \mathrm{i}k_n x}}{k_n^2(2\mu_n h + \sin(2\mu_n h))} + \sum_{n=N+1}^{\infty} \frac{4\mu_n^2 \sinh(\lambda_n b)\sin(\mu_n(z+h)) e^{\mp\lambda_n x}}{\lambda_n^2(2\mu_n h + \sin(2\mu_n h))}, \tag{38a}$$

$$\left.\frac{\partial\phi^0}{\partial z}\right|_{|x|<b} = -\frac{4\mu_0^2 \sinh(\mu_0(z+h)) e^{-\mathrm{i}k_0 b}\cos(k_0 x)}{k_0^2(2\mu_0 h + \sinh(2\mu_0 h))} + \sum_{n=1}^{N} \frac{4\mu_n^2 \sin(\mu_n(z+h)) e^{-\mathrm{i}k_n b}\cos(k_n x)}{k_n^2(2\mu_n h + \sin(2\mu_n h))} - \sum_{n=N+1}^{\infty} \frac{4\mu_n^2 e^{-\lambda_n b}\sin(\mu_n(z+h))\cosh(\lambda_n x)}{\lambda_n^2(2\mu_n h + \sin(2\mu_n h))} + \frac{\omega^2\cos(k_s z) - gk_s\sin(k_s z)}{gk_s\sin(k_s h) + \omega^2\cos(k_s h)}, \quad \left(k_s = \frac{\omega}{c}\right) \tag{38b}$$

The potential function matches with what was found by Yamamoto [8]. The horizontal (u) and vertical (v) velocity components can be obtained as

$$\boldsymbol{W} = \mathrm{i}\omega \left.\frac{\partial\phi^0}{\partial \boldsymbol{s}}\right|_{|x|\lessgtr b}, \quad \text{where} \quad \boldsymbol{W} = (u, v),\ \boldsymbol{s} = (x, z). \tag{39}$$

4.4. Shallow water approximation

The calculations we present are challenging to validate except in the shallow-water limit. We know the solution profile for shallow water can be calculated in a more straightforward alternative manner. Under the assumption of shallow water, the region-wise $f_m^c(x,\omega)$ can be written as

$$f_c^m(x,\omega)|_{|x|>b} = -b^2(-1)^m \frac{\mathrm{i}\mu_0^2 \sin(k_0 b) e^{\mp \mathrm{i}k_0 x}}{m^2\pi^2 - k_0^2 b^2}, \tag{40a}$$

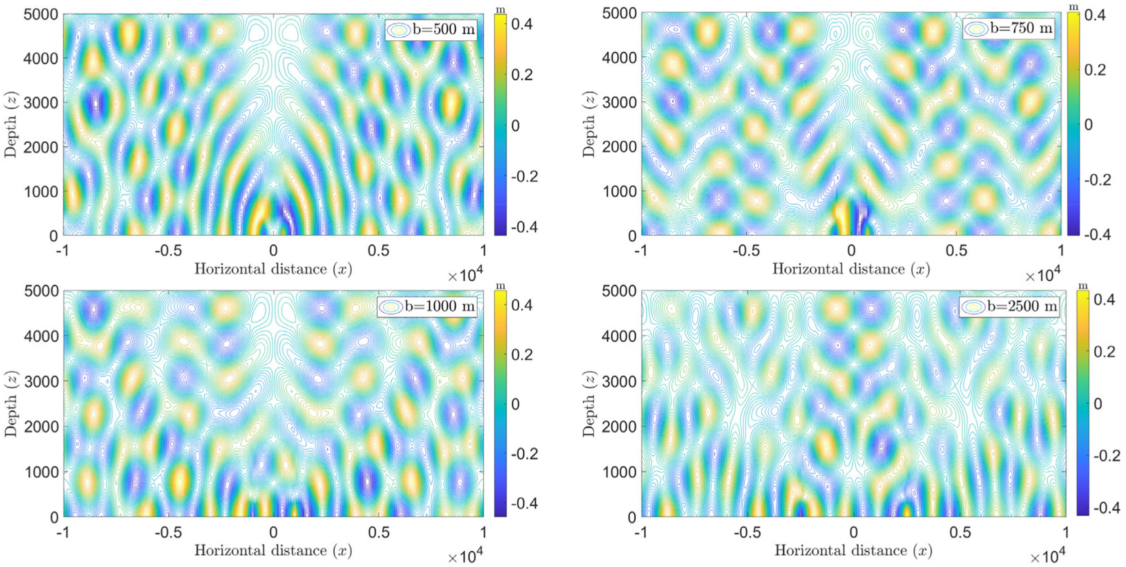

Fig. 4. Horizontal velocity components are plotted for $b = 500$, 750, 1000 and 2400 m. The angular frequency and ocean depth are fixed at $\omega = 2\pi$, $h = 5000$ m, respectively. Slanted stratified layers are found around the narrower fault, which become near-vertical away from the fault.

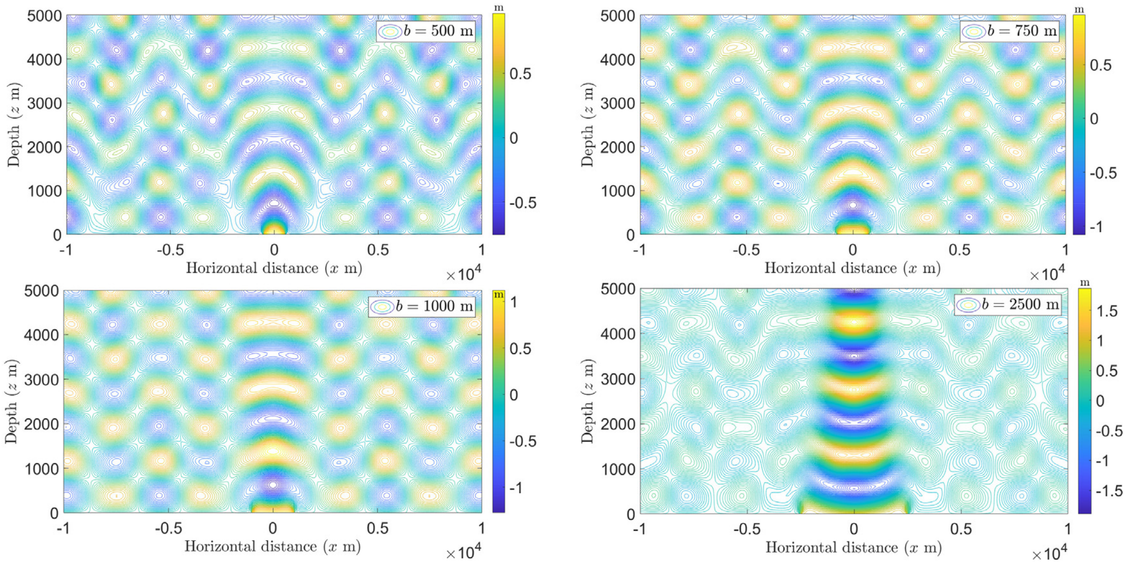

Fig. 5. Vertical velocity component for the same set of parameters considered in Fig. 4. Very high magnitude is observed in the water column above the wider fault. Velocity stratification above the fault is semi-circular for narrow faults and turns out to be more horizontal when fault width increases.

$$f_c^m(x,\omega)|_{|x|<b} = b^2(-1)^m \frac{\mu_0^2 \cos(k_0 x) e^{-\mathrm{i}k_0 b}}{m^2\pi^2 - k_0^2 b^2} - \frac{\omega^2 \cos(k_e x)}{g\xi_m^2 h - \omega^2}, \tag{40b}$$

where $k_0 = \omega/\sqrt{gh}$. An equivalent expressions for $f_m^s(x,\omega)$ are given by

$$f_s^m(x,\omega)|_{|x|>b} = (-1)^m bm\pi \frac{\mu_0^2 \sin(k_0 b) e^{\mp \mathrm{i}k_0 x}}{k_0(m^2\pi^2 - k_0^2 b^2)}, \tag{41a}$$

$$f_s^m(x,\omega)|_{|x|<b} = (-1)^m bm\pi \frac{\mu_0^2 \sin(k_0 x) e^{-\mathrm{i}k_0 b}}{k_0(m^2\pi^2 - k_0^2 b^2)} - \frac{\omega^2 \sin(k_e x)}{g\mu_e^2 h - \omega^2}. \tag{41b}$$

The surface elevation can be obtained using Eq. (34).

5. Numerical results

5.1. Time-harmonic solution of flat ocean bottom

The horizontal and vertical velocity components for four different values of width b, namely 500, 750, 1000 and 2500 m, of the oscillating bottom are plotted. The angular frequency is fixed at $\omega = 2\pi$ and the ocean depth at 5000 m.

The contour plot of the horizontal velocity component is shown in Fig. 4 for the same values of b mentioned in the previous graph. The locations of equal horizontal velocity occupy slanted vertical water columns for lower values of b and near the fault region. They tend to be almost vertical as b becomes larger. Consecutive regions of low and high horizontal velocity exist along the horizontal direction.

A similar contour plot for the vertical velocity component is shown in Fig. 5. A clear pattern of larger velocity amplitude is found in the water column just above the fault. The magnitude increases sufficiently for a larger fault width. The consecutive stratified layers of opposite velocity are more circular for smaller fault width, and they become flattened near the surface. Such layers just above the larger fault width are more flattened. Consecutive patches of the positive and negative velocity regions occur in horizontal and vertical directions far away from the fault region and are less influenced.

5.2. Time-dependent motion of the free surface

The method allows arbitrary bottom displacements and rise times to be simulated or more complicated combinations of these to be simulated. However, we present here some simple calculations. Note that the solution needs to be seen in the accompanying movie files to appreciate the complex motion. We take our scenario from [5] details of which will be given

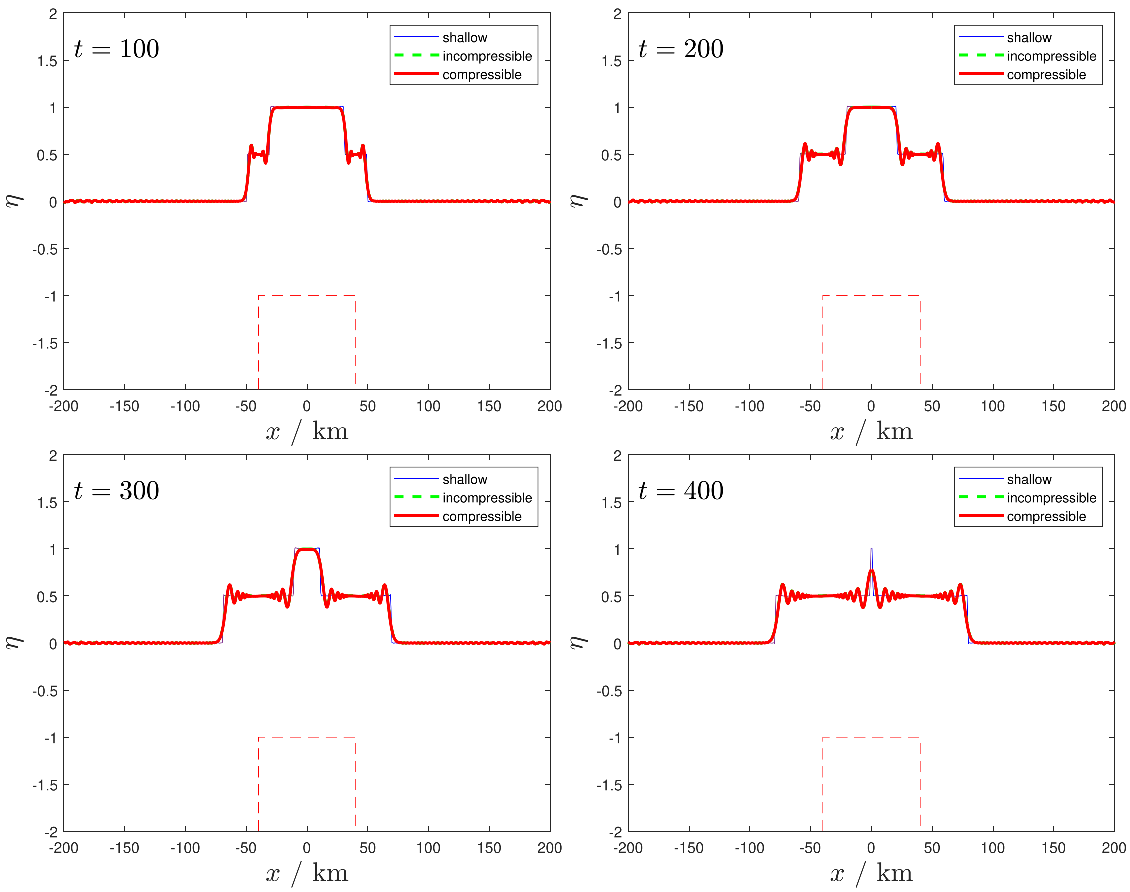

Fig. 6. The displacement of the free-surface for a flat bottom profile with τ = 10s, $b = 40$ km and $l_{\max} = 1$ for the times shown. The bottom displacement is shown as a red dashed line for illustration with the same vertical scale as the surface but plotted relative to negative two. The incompressible shallow water solution is also given and the incompressible solution. The depth is 1 km. The full animation can be found in movie 1. (For interpretation of the references to colour in this figure legend, the reader is referred to the web version of this article.)

shortly. For the computations which follow, we assume the growth rate is constant for a finite time τ, i.e.

$$l(t) = \frac{l_{\max} t}{\tau}\mathcal{H}(t(\tau - t)) + l_{\max}\mathcal{H}(t - \tau) \tag{42}$$

and in this case, the quantity $\mathcal{W}(\omega, \tau)$ takes the following simple form:

$$\mathcal{W}(\omega, \tau) = l_{\max}\frac{\left(e^{-\mathrm{i}\omega\tau} - 1\right)}{\tau\omega^2}. \tag{43}$$

For the numerical calculations which follow we will assume $\tau = 10$s and $l_{\max} = 1$, following [5].

We assume that $b = 40$ km, again following [5]. Other scenarios are shown in the supplementary material. The exact solution can be found for shallow water for $m = 0$ forcing, i.e. $\mathcal{X}$ is a constant, which is given in Appendix B.

The displacement of the free surface is best viewed as movies that are supplied as supplementary material. Figures 6 to 8 are solutions for $\mathcal{X} = 1$. They show the displacement of the free surface for shallow incompressible water, incompressible water and compressible water. The dotted line shows the ocean bottom displacement, which is drawn for illustration only. The ocean depth is assumed 1 km in Fig. 6, where we also consider a simple flat profile. The effect of compressibility is small here, and no AGW can be seen. The shallow water approximation works well. In Figs. 7 and 8 the depth is increased to 4 km, again as used in [5]. In Fig. 7 where we also consider a simple flat profile, while in Fig. 8, we consider a Gaussian profile with

$$\mathcal{X} = \exp(-6(x/40000)^2) \tag{44}$$

We calculate the coefficients ζ_m^c from the well-known Fourier series formula.

The movies show a number of striking features, including a very strong dependence on depth to see the effect of the compressibility and the existence of a compressive wave that propagates vertically with a period of four times the depth divided by the acoustic speed. The rapidly propagating AGW, proposed as a mechanism to predict tsunamis, is also apparent. The purpose of the present work is not to exhaustively describe the complex emotions which arise. We provide the computer code used to generate the figures to motivate others in further investigations in the supplementary material. However, we

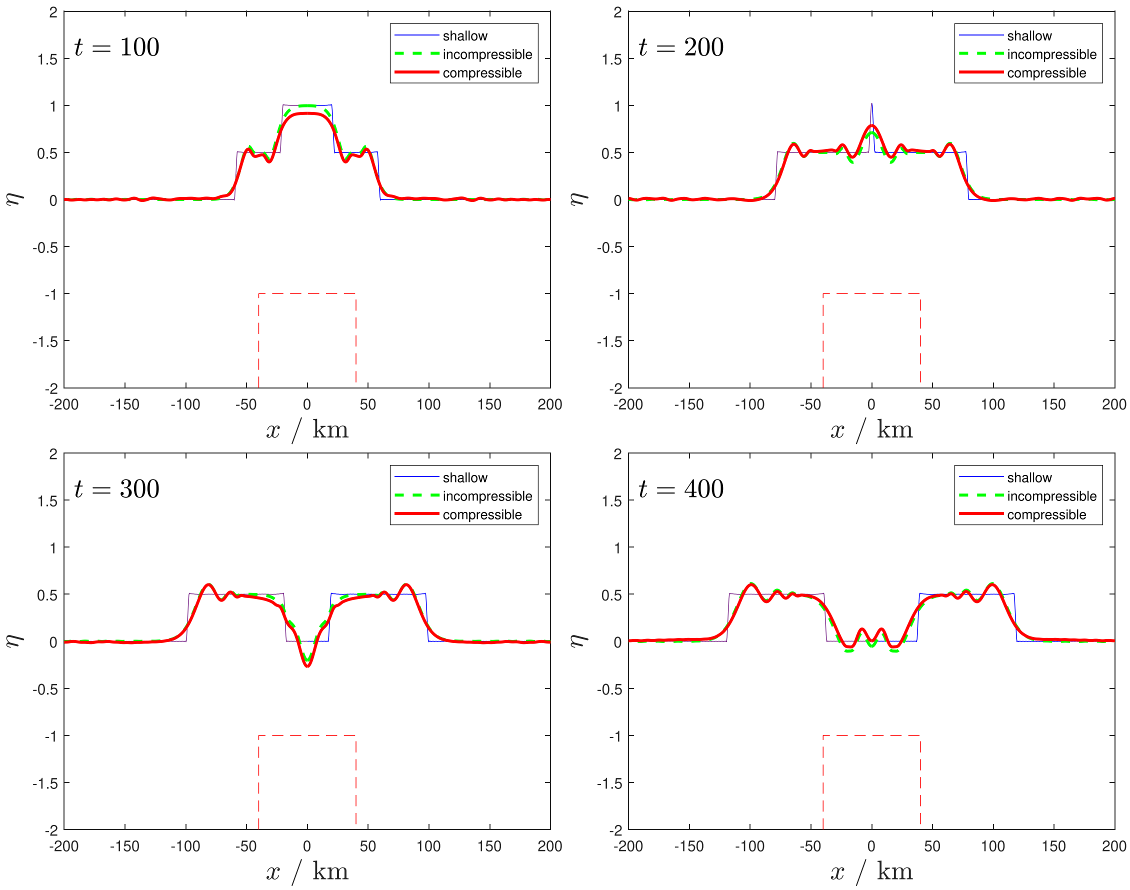

Fig. 7. As in Fig. 6 except the depth is 4 km. The full animation can be found in movie 2.

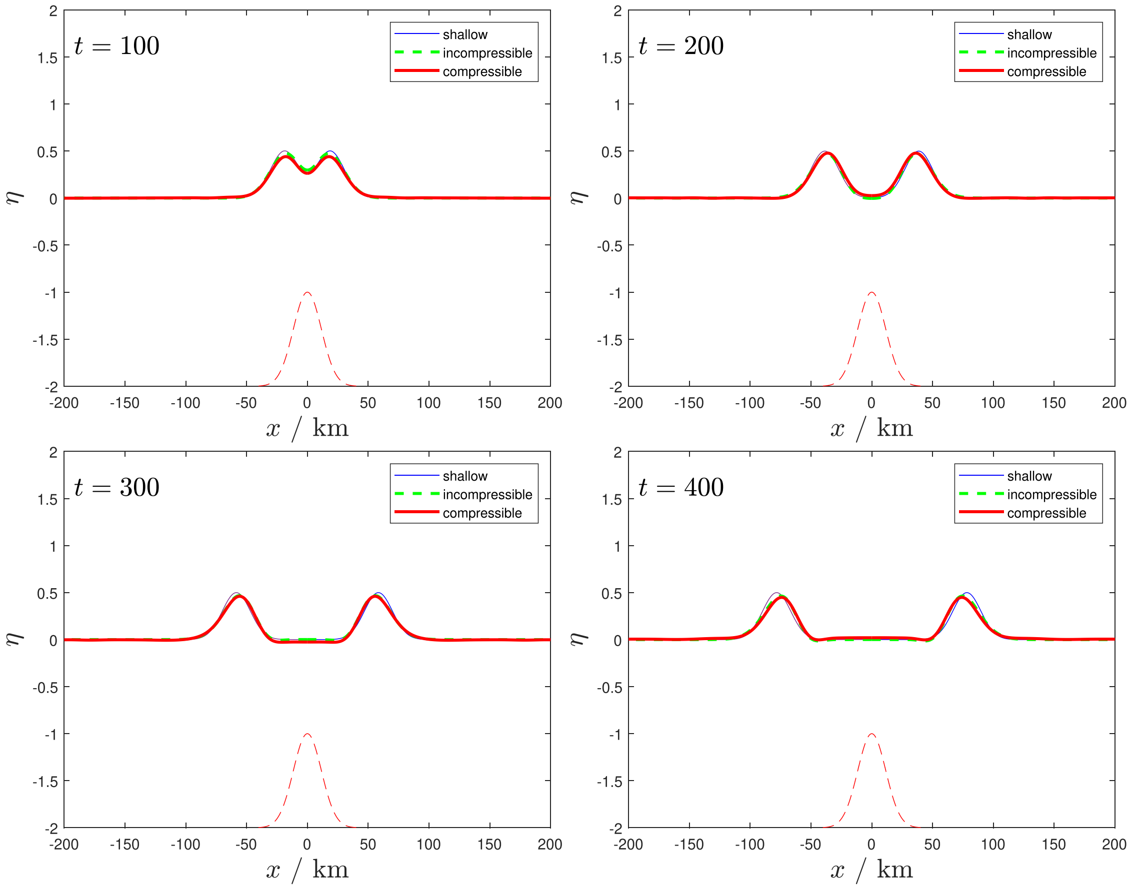

Fig. 8. As in Fig. 6 except the bottom displacement is given by (44) and the depth is 4 km. The full animation can be found in movie 3.

believe that this phenomenon in which the entire ocean surface oscillates has not been reported previously. We believe that this could be a method to predict tsunamis; however, we note that this oscillation required a sufficiently deep ocean or rapid sea floor rise.

The results in Fig. 8 are closely related to those given in [5]. However, in that paper, the focus was on the far field wave, and they only calculated the response at $X = 1000$ km and after a larger time than we show here. From the associated movie file, we can see that the AGW are generated there as an initial oscillation of the ocean surface. Detection of this oscillation may be a possible method to detect tsunamis. It may be noted that the static compression is neglected in this work unlike the work by [33] where its impact on the long wave range is shown. Inclusion of this effect would result in $0.5 - 1\%$ error, depending upon the ocean depth, in the phase speed as well as in the near-field surface elevation. More detailed analysis of this can be found in Appendix C. Recently, [40] have shown that the mathematical model where static compression is ignored led to good matching with the measured field data for a relatively short time. We acknowledge that a further detailed study is required to ascertain fully the effect of static compression.

6. Conclusion

Within the linear water wave theory framework, the generation of acoustic-gravity waves due to the vertical oscillation of seafloor having a sinusoidal surface is studied. A closed-form solution for the velocity potential is obtained using the Fourier transformation technique, which is utilised to find the surface profile for the case when the fault rises for a finite time. This form is generic, and other profiles, including the flat surface case, can be approximated. The time-dependent solution of the sinusoidal case is utilised to depict the surface wave profiles due to flat and Gaussian-type raised ocean floor. The simulations show the surface wave propagation imitating the tsunami wave generation at the surface over the raised seafloor and its propagation away from the source origin. A clear distinction between the surface wave profile for the compressible and incompressible ocean is shown for different types of ocean bottom profiles. The time-harmonic solution corresponding to the flat surface fault is utilised to compute velocity profiles. The horizontal velocity profile around the fault shows slanted water columns of equal properties, which becomes near-vertical away from the fault. However, the vertical velocity component has a very high magnitude above the wider fault. In the case of a narrow fault, semi-circular stratified layers are found close to the fault. The near field time domain calculations show that when the acoustic gravity waves are generated, they lead to a rapid oscillation of the fluid surface. We also show that significant AGW are generated only for sufficiently deep water for a given rise time.

Author's contribution

SD conceptualised the problem and solved the mathematical problem analytically with help from MHM. The computational results for the time-harmonic solution are generated by SD, whereas the time-dependent results are provided by MHM. The manuscript is written by SD in consultation with MHM.

Declaration of Competing Interest

The authors report no conflict of interest

Data availability

No experimental data are involved in this work. The computer code used to generate the figures is provided.

Acknowledgement

No research funding is involved in this study. Both SD and MHM acknowledge the support received from the host Institute/University to carry out the research.

Appendix A. Solution using eigenfunction matching for $m = 0$

Since the mathematical problem is symmetric across $x = 0$, we shall solve it in the region $x > 0$ and utilise the symmetry to calculate the displacement potential function in the region $x < 0$. The region $x > 0$ is divided into two parts, namely $x > b$ and $0 < x < b$. The potential function in the region $x > b$ can be written as

$$f_1(x,z) = a_0 \frac{\cosh \mu_0(z+h)}{\cosh \mu_0 h} e^{-\mathrm{i}k_0(x-b)} + \sum_{n=1}^{N} a_n \frac{\cos \mu_n(z+h)}{\cos \mu_n h} e^{-\mathrm{i}k_n(x-b)} + \sum_{n=N+1}^{\infty} a_n \frac{\cos \mu_n(z+h)}{\cos \mu_n h} e^{-\lambda_n(x-b)}. \tag{A.1}$$

Likewise, the potential function in $0 < x < b$ can be written as

$$\begin{aligned} f_2(x,z) =& b_0 \frac{\cosh \mu_0(z+h)}{\cosh \mu_0 h} \frac{\cos k_0 x}{\cos k_0 b} + \sum_{n=1}^{N} b_n \frac{\cos \mu_n(z+h)}{\cos \mu_n h} \frac{\cos k_n x}{\cos k_n b} \\ &+ \sum_{n=N+1}^{\infty} b_n \frac{\cos \mu_n(z+h)}{\cos \mu_n h} \frac{\cosh \lambda_n x}{\cosh \lambda_n b} + \frac{k_s \cos k_s z + \frac{\omega^2}{g} \sin k_s z}{k_s\left(\frac{\omega^2}{g} \cos k_s h + k_s \sin k_s h\right)}. \end{aligned} \tag{A.2}$$

The above forms can be symbolically written as

$$f_1(x,z) = \sum_{n=0}^{\infty} a_n \frac{\cos \alpha_n(z+h)}{\cos \alpha_n h} e^{-\delta_n(x-b)},$$

$$f_2(x,z) = \sum_{n=0}^{\infty} b_n \frac{\cos \alpha_n(z+h)}{\cos \alpha_n h} \frac{\cosh \delta_n x}{\cosh \delta_n b} + \frac{k_s \cos k_s z + \frac{\omega^2}{g} \sin k_s z}{k_s\left(\frac{\omega^2}{g} \cos k_s h + k_s \sin k_s h\right)},$$

along with the dispersion relation

$$\frac{\omega^2}{g} = -\alpha_n \tanh \alpha_n h, \tag{A.3}$$

where $(\alpha_0, \delta_0) = (\mathrm{i}\mu_0, \mathrm{i}k_0)$, $(\alpha_n, \delta_n) = (\mu_n, \mathrm{i}k_n)$ for $n = 1, \ldots, N$ and $(\alpha_n, \delta_n) = (\mu_n, \lambda_n)$ for $n = N+1, \ldots$.

Now using the matching of potential and its derivative along $x = b$,

$$\sum_{n=0}^{\infty} b_n \frac{\cos \alpha_n(z+h)}{\cos \alpha_n h} + \frac{k_s \cos k_s z + \frac{\omega^2}{g} \sin k_s z}{k_s\left(\frac{\omega^2}{g} \cos k_s h + k_s \sin k_s h\right)} = \sum_{n=0}^{\infty} a_n \frac{\cos \alpha_n(z+h)}{\cos \alpha_n h}$$

$$\text{and}\quad \sum_{n=0}^{\infty} b_n\delta_n \frac{\cos\alpha_n(z+h)}{\cos\alpha_n h}\tanh\delta_n b = \sum_{n=0}^{\infty} -a_n\delta_n \frac{\cos\alpha_n(z+h)}{\cos\alpha_n h}$$

Using the orthogonality relation of α_n, the above two equations provides:

$$(a_n - b_n)\int_{-h}^{0} \frac{\cos^2\alpha_n(z+h)}{\cos^2\alpha_n h}dz = \int_{-h}^{0} \frac{k_s\cos k_s z + \frac{\omega^2}{g}\sin k_s z}{k_s\left(\frac{\omega^2}{g}\cos k_s h + k_s\sin k_s h\right)}\frac{\cos\alpha_n(z+h)}{\cos\alpha_n h}dz, \tag{A.4}$$

$$b_n\tanh\delta_n b = -a_n, \tag{A.5}$$

solving which we obtain the unknowns a_n and b_n. Simplifying Eq. (A.4) using the dispersion relation $\frac{\omega^2}{g} = -\alpha_n\tanh\alpha_n h$, we obtain

$$a_n - b_n = \frac{4\alpha_n\cos\alpha_n h}{(k_s^2 - \alpha_n^2)(2\alpha_n h + \sin 2\alpha_n h)} \tag{A.6}$$

Now we consider the three following cases:

A1. Case I: $n = 0$

This case corresponds to the propagating gravity mode with $\alpha_0 = \mathrm{i}\mu_0$ and $\delta_0 = \mathrm{i}k_0$. The dispersion relation takes the form $\frac{\omega^2}{g} = \mu_0\tanh\mu_0 h$. The system of equations (A.5 and A.6) take the following form:

$$a_0 = -\mathrm{i}b_0\tan k_0 b, \quad \text{and} \quad a_0 - b_0 = \frac{4\mu_0\cosh\mu_0 h}{k_0^2(2\mu_0 h + \sinh 2\mu_0 h)},$$

solving which we obtain

$$a_0 = \frac{4\mathrm{i}\mu_0\cosh\mu_0 h\sin k_0 b}{k_0^2(2\mu_0 h + \sinh 2\mu_0 h)}e^{-\mathrm{i}k_0 b} \quad \text{and} \quad b_0 = -\frac{4\mu_0\cosh\mu_0 h\cos k_0 b}{k_0^2(2\mu_0 h + \sinh 2\mu_0 h)}e^{-\mathrm{i}k_0 b}. \tag{A.7}$$

A2. Case II: $n = 1, \ldots, N$

This case corresponds to the acoustic-gravity modes and the corresponding dispersion relation takes the form $\frac{\omega^2}{g} = -\mu_n\tan\mu_n h$. We consider $\alpha_n = \mu_n$ and $\delta_n = \mathrm{i}k_n$. Applying a similar approach, the coefficients a_n and b_n are expressed as

$$a_n = \frac{4\mathrm{i}\mu_n\cos\mu_n h\sin k_n b}{k_n^2(2\mu_n h + \sin 2\mu_n h)}e^{-\mathrm{i}k_n b} \quad \text{and} \quad b_n = -\frac{4\mu_n\cosh\mu_n h\cos k_n b}{k_n^2(2\mu_n h + \sin 2\mu_n h)}e^{-\mathrm{i}k_n b}. \tag{A.8}$$

A3. Case III: $n = N+1, \ldots$

This case corresponds to the evanescent modes and the corresponding dispersion relation takes the form $\frac{\omega^2}{g} = -\mu_n\tan\mu_n h$. We consider $\alpha_n = \mu_n$ and $\delta_n = \lambda_n$. Applying a similar approach, the coefficients a_n and b_n are expressed as

$$a_n = -\frac{4\mu_n\cos\mu_n h\sinh\lambda_n b}{\lambda_n^2(2\mu_n h + \sin 2\mu_n h)}e^{-\lambda_n b} \quad \text{and} \quad b_n = \frac{4\mu_n\cosh\mu_n h\cosh\lambda_n b}{\lambda_n^2(2\mu_n h + \sin 2\mu_n h)}e^{-\lambda_n b}. \tag{A.9}$$

Putting the expressions of a_n and b_n ($n = 0, 1, \ldots$) from Eqs. (A.7)-(A.9) back into Eqs. (A.3) and (A.3), we are able to retrieve the form of the potential functions obtained using the Fourier Transformation technique (see [8]). The same equations can also be derived from the expressions (30) and (31) after putting $m = 0$.

Appendix B. Shallow water incompressible ocean for $m = 0$

We consider here the time-domain case of shallow water with $m = 0$. We focus on the region $x > 0$, and the solution for $x < 0$ can be obtained from the symmetry. Here the displacement potential is written as

$$\Phi(x,z,t) = \frac{1}{2\pi}\int_{-\infty}^{\infty}\phi(x,z,\omega)e^{\mathrm{i}\omega t}d\omega,$$

where

$$\phi(x,z,\omega)|_{0<x<b} = \frac{e^{-i\omega\tau}-1}{\tau\omega^2}\left\{\frac{-\cosh k_0(z+h)\cos(k_0x)e^{-ik_0b}}{k_0^2h} + \left(z+\frac{g}{\omega^2}\right)\right\}, \tag{B.1a}$$

$$\phi(x,z,\omega|_{x>b}) = \frac{e^{-i\omega\tau}-1}{\tau\omega^2}\frac{i\cosh k_0(z+h)\sin(k_0b)e^{-ik_0x}}{k_0^2h}. \tag{B.1b}$$

where k_0 satisfies the dispersion relation

$$\frac{\omega^2}{g} = k_0^2h.$$

B1. Instantaneous displacement

We derive here the well-known solution for an instantaneous displacement. This is a common assumption used to model tsunami waves, and this provides some confidence in our solution for the more general case. We take the limit as $\tau \to 0$, and we have a single root $\sqrt{gh}k_0 = \omega$. Under the shallow water approximation of the free surface displacement can be written as

$$\begin{aligned}\eta(x,t)|_{0<x<b} &= \frac{1}{2\pi}\int_{-\infty}^{\infty}\frac{-i}{\omega}\left\{-e^{-ik_0b}\cos(k_0x)+1\right\}e^{i\omega t}d\omega,\\ &= \frac{1}{2\pi}\int_{-\infty}^{\infty}\frac{-i}{\omega}\left\{-e^{-i\omega b/\sqrt{gh}}\cos(\omega x/\sqrt{gh})+1\right\}e^{i\omega t}d\omega,\end{aligned} \tag{B.2a}$$

$$\begin{aligned}\eta(x,t)|_{x>b} &= \frac{1}{2\pi}\int_{-\infty}^{\infty}-\frac{i}{\omega}\left\{i\sin(k_0b)e^{-ik_0x}\right\}e^{i\omega t}d\omega,\\ &= \frac{1}{2\pi}\int_{-\infty}^{\infty}\frac{1}{\omega}\left\{\sin(\omega b/\sqrt{gh})e^{-i\omega x/\sqrt{gh}}\right\}e^{i\omega t}d\omega.\end{aligned} \tag{B.2b}$$

We further simplify the above expressions in the following manner:

$$\begin{aligned}\eta(x,t)|_{0<x<b} &= \frac{1}{2\pi}\fint_{-\infty}^{\infty}\frac{-i}{\omega}\left\{-e^{-i\omega b/\sqrt{gh}}\cos(\omega x/\sqrt{gh})+1\right\}e^{i\omega t}d\omega,\\ &= \frac{1}{2\pi}\lim_{a\to 0}\left[\left(\int_{\infty}^{-a}+\fint_{-a}^{a}+\int_{a}^{\infty}\right)\frac{(-i)}{\omega}\left\{-e^{-i\omega b/\sqrt{gh}}\cos(\omega x/\sqrt{gh})+1\right\}e^{i\omega t}d\omega\right],\\ &= \frac{1}{2\pi}\left[-\pi i\,\mathrm{Res}(x,0) + \fint_{-\infty}^{\infty}\frac{(-i)}{\omega}\left\{-e^{-i\omega b/\sqrt{gh}}\cos(\omega x/\sqrt{gh})+1\right\}e^{i\omega t}d\omega\right],\\ &= \frac{1}{2\pi}\fint_{-\infty}^{\infty}\frac{(-i)}{\omega}\left\{-e^{-i\omega b/\sqrt{gh}}\cos(\omega x/\sqrt{gh})+1\right\}e^{i\omega t}d\omega,\ \ (\text{since } \mathrm{Res}(x,0)=0).\end{aligned} \tag{B.3}$$

where $\fint$ represents the Cauchy Principal Value of the integral, $\fint$ represents contour integration using the path that includes the singularity at $\omega = 0$ from above and involves the lower half of the complex plane, i.e., $(\omega) < 0$ with representing the imaginary part of a complex number, and $\mathrm{Res}(x,0)$ represents the residue of the integrand at the point $\omega = 0$. Similarly,

$$\begin{aligned}\eta(x,t)|_{x>b} &= \frac{1}{2\pi}\fint_{-\infty}^{\infty}\frac{1}{\omega}\left\{\sin(\omega b/\sqrt{gh})e^{-i\omega x/\sqrt{gh}}\right\}e^{i\omega t}d\omega, \quad x>b,\\ &= \frac{1}{2\pi}\left[-\pi i\,\mathrm{Res}(x,0) + \fint_{-\infty}^{\infty}\frac{1}{\omega}\left\{\sin(\omega b/\sqrt{gh})e^{-i\omega x/\sqrt{gh}}\right\}e^{i\omega t}d\omega\right],\\ &= \frac{1}{2\pi}\fint_{-\infty}^{\infty}\frac{1}{\omega}\left\{\sin(\omega b/\sqrt{gh})e^{-i\omega x/\sqrt{gh}}\right\}e^{i\omega t}d\omega, \quad (\text{since } \mathrm{Res}(x,0)=0).\end{aligned} \tag{B.4}$$

Here, we shall apply the following expression to compute the surface displacement with the help of the Heaviside function

$$\frac{1}{2\pi i}\fint_{-\infty}^{\infty}\frac{e^{-i\omega t}}{\omega}d\omega = H(t), \quad t>0, \tag{B.5}$$

Then the region-wise surface displacements are written as

$$\eta(x,t)|_{0<x<b} = -\frac{1}{2}\left[H\left(t+\frac{x-b}{\sqrt{gh}}\right)+H\left(t-\frac{x+b}{\sqrt{gh}}\right)\right]+H(t),$$
$$= \frac{1}{2}\Big[H(x-t\sqrt{gh}+b)-H(x-t\sqrt{gh}-b)+H(x+t\sqrt{gh}+b)-H(x+t\sqrt{gh}-b)\Big]. \tag{B.6a}$$

$$\eta(x,t)|_{x>b} = \frac{1}{2}H(x-t\sqrt{gh}+b)-\frac{1}{2}H(x-t\sqrt{gh}-b). \tag{B.6b}$$

It is quite astonishing to notice that the free surface displacement is a smooth function, and the integral is computable using Cauchy Principal Value.

B2. Finite time displacement

Now we consider the case when τ is finite and the corresponding expressions of free surface elevation become

$$\eta(x,t)|_{0<x<b} = \frac{1}{2\pi}\int_{-\infty}^{\infty}\frac{e^{-\mathrm{i}\omega\tau}-1}{\tau\omega^2}\left\{-e^{-\mathrm{i}\omega b/\sqrt{gh}}\cos(\omega x/\sqrt{gh})+1\right\}e^{\mathrm{i}\omega t}d\omega,$$
$$= \frac{1}{2\pi}\left[\int_{-\infty}^{\infty}\frac{-1}{2\tau\omega^2}\left(e^{\mathrm{i}\omega(t-\tau)}-e^{\mathrm{i}\omega t}\right)\left(e^{-\mathrm{i}\omega(b-x)/\sqrt{gh}}+e^{-\mathrm{i}\omega(b+x)\sqrt{gh}}-2\right)d\omega\right], \tag{B.7}$$

and

$$\eta(x,t)|_{x>b} = \frac{1}{2\pi}\int_{-\infty}^{\infty}\frac{e^{-\mathrm{i}\omega\tau}-1}{\tau\omega^2}\left\{\mathrm{i}\sin(\omega b/\sqrt{gh})e^{-\mathrm{i}\omega x/\sqrt{gh}}\right\}e^{\mathrm{i}\omega t}d\omega,$$
$$= \frac{1}{2\pi}\left[\int_{-\infty}^{\infty}\frac{1}{2\tau\omega^2}\left(e^{\mathrm{i}\omega(t-\tau)}-e^{\mathrm{i}\omega t}\right)\left(e^{-\mathrm{i}\omega(x-b)/\sqrt{gh}}-e^{-\mathrm{i}\omega(x+b)\sqrt{gh}}\right)d\omega\right], \tag{B.8}$$

Here, we shall apply (B.5) and the following expression to compute the surface displacement with the help of Heaviside function

$$\frac{1}{2\pi}\int_{-\infty}^{\infty}\frac{e^{-\mathrm{i}\omega t}}{\omega^2}d\omega = tH(t), \quad t>0, \tag{B.9}$$

Then the region-wise surface displacements are expressed as

$$\eta(x,t)|_{0<x<b} = \frac{1}{2\tau}\Bigg[2(\tau-t)H(\tau-t)-2(-t)H(-t)-\left(\frac{b-x}{\sqrt{gh}}-t+\tau\right)H\left(\frac{b-x}{\sqrt{gh}}-t+\tau\right)$$
$$+\left(\frac{b-x}{\sqrt{gh}}-t\right)H\left(\frac{b-x}{\sqrt{gh}}-t\right)-\left(\frac{b+x}{\sqrt{gh}}-t+\tau\right)H\left(\frac{b+x}{\sqrt{gh}}-t+\tau\right)$$
$$+\left(\frac{b+x}{\sqrt{gh}}-t\right)H\left(\frac{b+x}{\sqrt{gh}}-t\right)\Bigg] \tag{B.10}$$

$$\eta(x,t)|_{x>b} = \frac{1}{2\tau}\Bigg[-\left(\frac{x+b}{\sqrt{gh}}-t+\tau\right)H\left(\frac{x+b}{\sqrt{gh}}-t+\tau\right)+\left(\frac{x-b}{\sqrt{gh}}-t+\tau\right)H\left(\frac{x-b}{\sqrt{gh}}-t+\tau\right)$$
$$-\left(\frac{x-b}{\sqrt{gh}}-t\right)H\left(\frac{x-b}{\sqrt{gh}}-t\right)+\left(\frac{x+b}{\sqrt{gh}}-t\right)H\left(\frac{x+b}{\sqrt{gh}}-t\right)\Bigg]. \tag{B.11}$$

Appendix C. Effect of static compression of the ocean water

A few recent works in the context of the present physical problem have included the effect of static ocean compressibility into the system (e.g. [33]). Such a modification results in the new dispersion relation

$$\frac{\omega^2}{g} = \hat{\mu}_n\frac{\left(1-\left(\frac{\gamma}{2\hat{\mu}_n}\right)^2\right)\tanh(\hat{\mu}_n h)}{1-\left(\frac{\gamma}{2\hat{\mu}_n}\right)\tanh(\hat{\mu}_n h)}, \tag{C.1}$$

where $\hat{\mu}_n^2 = \mu_n^2+\gamma^2/4$ and $\gamma = g/c^2$ is the parameter representing the static compression.

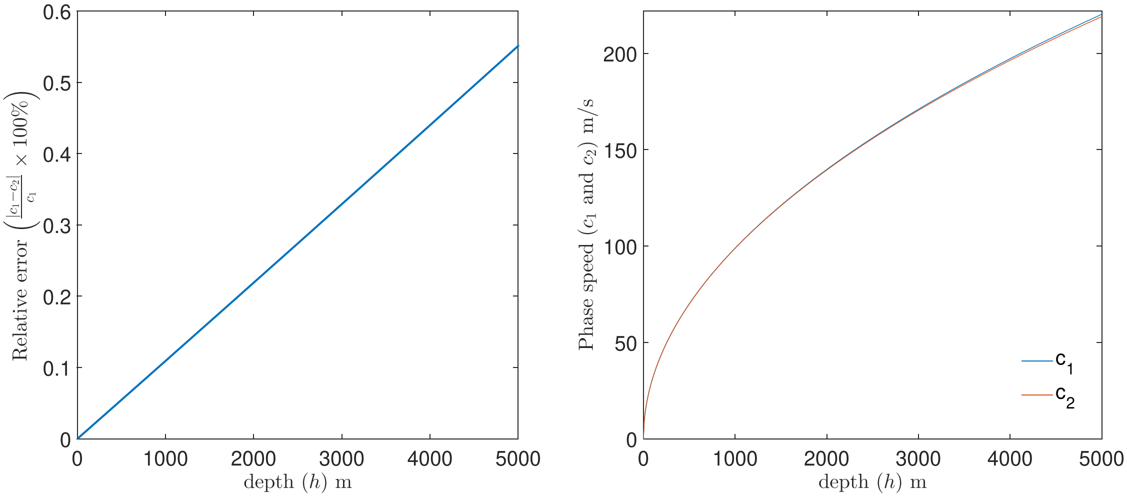

Fig. C1. The relative error in computing the phase speed of the surface gravity wave is presented in the left panel when the static ocean water compression is ignored. The maximum relative error is 0.55% up to 5000 m ocean depth. The phase speed c_1 and c_2 are shown in the right panel.

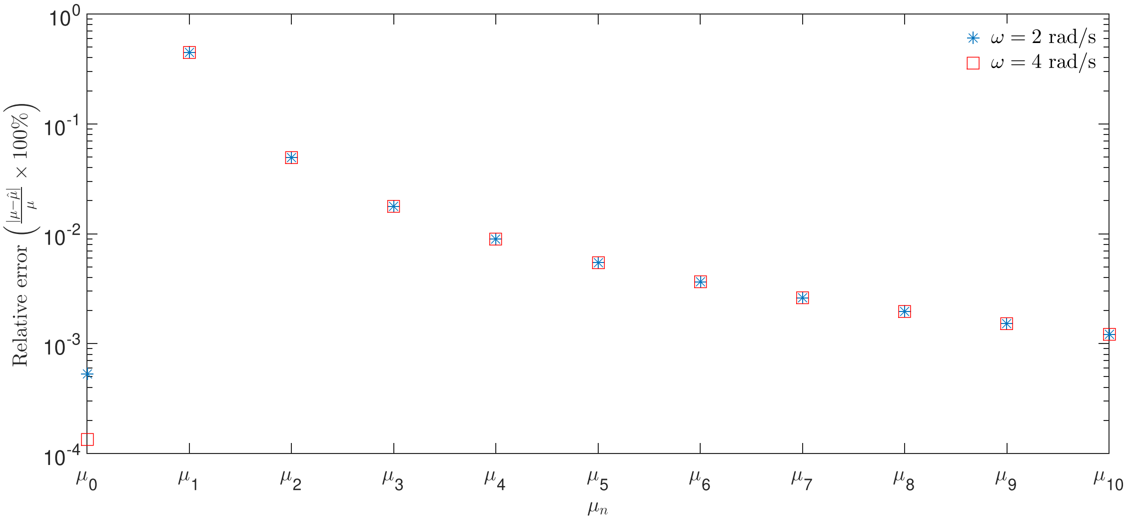

Fig. C2. The relative error in computing the wavenumber μ is shown in a surface plot within a frequency range of 0.0001 – 10 rad/s taken, and for the surface gravity and the first 10 evanescent modes. The maximum relative error obtained is 0.5%.

Under the shallow water approximation, the corresponding phase speed of the surface gravity waves (from (22) or equivalently by putting $\gamma = 0$ in the above equation) turns out to be

$$C_1 = \sqrt{gh}\left(1 - \frac{1}{4}M^2\right), \tag{C.2}$$

where $M = \sqrt{gh}/c$. Now the corresponding phase speed of the surface gravity wave in the absence of static compression leads to

$$C_2 = \sqrt{gh}\left(1 - \frac{1}{2}M^2\right). \tag{C.3}$$

The corresponding relative error $\frac{|c_1 - c_2|}{c_2} \times 100\%$ is plotted in the Fig. C.9 for water depth up to 4000 m. The figure clearly shows the relative error below 0.55%. The phase speed is a monotonically increasing function of ocean depth, and the computed maximum values are $c_1 = 220.2653$ m/s and $c_2 = 219.0583$ m/s.

We compute wavenumbers μ_n at $h = 5000$ m using both (C.1) and (22). The relative error in computing the values of μ is defined by $\dfrac{|\mu - \hat{\mu}|}{\mu} \times 100\%$. The values of $N = 0, 1, \ldots, 10$ for the frequencies $\omega = 2, 4$ rad/s are considered. The result is shown in Fig. C.10, which provides a maximum error of 0.5% in the computation. In addition, the error in the computation of evanescent modes for two values of frequencies is small.

Supplementary material

Supplementary material associated with this article can be found, in the online version, at doi:10.1016/j.apm.2023.01.030.

References

[1] B.W. Levin, M. Nosov, et al., Physics of Tsunamis, Vol. 327, Springer, 2009.
[2] T. Maeda, T. Furumura, FDM simulation of seismic waves, ocean acoustic waves, and tsunamis based on tsunami-coupled equations of motion, Pure Appl. Geophys. 170 (1) (2013) 109–127.
[3] T.C.A. Oliveira, U. Kadri, Pressure field induced in the water column by acoustic-gravity waves generated from sea bottom motion, J. Geophys. Res-Oceans 121 (10) (2016) 7795–7803.
[4] M.A. Nosov, Tsunami generation in compressible ocean, Phys. Chem. Earth Pt. B 24 (5) (1999) 437–441.
[5] M. Stiassnie, Tsunamis and acoustic-gravity waves from underwater earthquakes, J. Eng. Math. 67 (1–2) (2010) 23–32.
[6] E.A. Okal, P.-J. Alasset, O. Hyvernaud, F. Schindelé, The deficient t waves of tsunami earthquakes, Geophys. J. Int. 152 (2) (2003) 416–432.
[7] L. Novikova, L. Ostrovsky, Excitation of tsunami waves by a traveling displacement of the ocean bottom, Mar. Geod. 2 (4) (1979) 365–380.
[8] T. Yamamoto, Gravity waves and acoustic waves generated by submarine earthquakes, Int. J. Soil Dyn. Earthq. Eng. 1 (2) (1982) 75–82.
[9] G. Rousseaux, P. Maïssa, C. Mathis, P. Coullet, T.G. Philbin, U. Leonhardt, Horizon effects with surface waves on moving water, New J. Phys. 12 (9) (2010) 095018.
[10] S. Das, T. Sahoo, M.H. Meylan, Dynamics of flexural gravity waves: from sea ice to Hawking radiation and analogue gravity, Proc. R. Soc. A 474 (2209) (2018) 20170223.
[11] M.S. Longuet-Higgins, A theory of the origin of microseisms, Philos. Tr. R. Soc. S-A 243 (857) (1950) 1–35.
[12] U. Kadri, Deep ocean water transport by acoustic-gravity waves, J. Geophys. Res-Ocean 119 (11) (2014) 7925–7930.
[13] A. Abdolali, U. Kadri, W. Parsons, J.T. Kirby, On the propagation of acoustic-gravity waves under elastic ice sheets, J. Fluid Mech. 837 (2018) 640–656.
[14] U. Kadri, M. Stiassnie, Acoustic-gravity waves interacting with the shelf break, J. Geophys. Res-Ocean 117 (C3) (2012).
[15] U. Kadri, M. Stiassnie, Generation of an acoustic-gravity wave by two gravity waves, and their subsequent mutual interaction, J. Fluid Mech. 735 (2013) R6.
[16] U. Kadri, T.R. Akylas, On resonant triad interactions of acoustic–gravity waves, J. Fluid Mech. 788 (2016) R1.
[17] U. Kadri, Triad resonance between a surface-gravity wave and two high frequency hydro-acoustic waves, Eur. J. Mech. B-Fluid. 55 (2016) 157–161.
[18] M. Tian, U. Kadri, Wavemaker theories for acoustic–gravity waves over a finite depth, J. Eng. Math. 108 (1) (2018) 25–35.
[19] U. Kadri, Tsunami mitigation by resonant triad interaction with acoustic–gravity waves, Heliyon 3 (1) (2017) e00234.
[20] U. Kadri, Acoustic-gravity waves interacting with a rectangular trench, Int. J. Geophysics 2015 (2015) 806834.
[21] L.M. Brekhovskikh, Y.P. Lysanov, R.T. Beyer, Fundamentals of ocean acoustics, 1991.
[22] E. Eyov, A. Klar, U. Kadri, M. Stiassnie, Progressive waves in a compressible-ocean with an elastic bottom, Wave Motion 50 (5) (2013) 929–939.
[23] A. Abdolali, J.T. Kirby, G. Bellotti, Depth-integrated equation for hydro-acoustic waves with bottom damping, J. Fluid Mech. 766 (2015) R1.
[24] R.D. Stoll, Acoustic waves in ocean sediments, Geophysics 42 (4) (1977) 715–725.
[25] F. Chierici, L. Pignagnoli, D. Embriaco, Modeling of the hydroacoustic signal and tsunami wave generated by seafloor motion including a porous seabed, J. Geophys. Res. Oceans 115 (C3) (2010).
[26] C.C.L. Sells, The effect of a sudden change of shape of the bottom of a slightly compressible ocean, Philos. Tr. R. Soc. S-A 258 (1092) (1965) 495–528.
[27] H. Miyoshi, Generation of the tsunami in compressible water (Part I), J. Oceanogr. Soc. Japan 10 (1) (1954) 1–9.
[28] M.A. Nosov, S.N. Skachko, Nonlinear tsunami generation mechanism, Nat. Hazard. Earth Sys. 1 (2001) 251–253.
[29] M.A. Nosov, S.V. Kolesov, Elastic oscillations of water column in the 2003 Tokachi-oki tsunami source: in-situ measurements and 3-D numerical modelling, Nat. Hazard. Earth Sys. 7 (2) (2007).
[30] U. Kadri, Wave motion in a heavy compressible fluid: revisited, Eur. J. Mech. B-Fluid 49 (2015) 50–57.
[31] S. Watada, S. Kusumoto, K. Satake, Traveltime delay and initial phase reversal of distant tsunamis coupled with the self-gravitating elastic earth, J. Geophysical Res: Solid Earth 119 (5) (2014) 4287–4310.
[32] A. Bagheri, S. Greenhalgh, A. Khojasteh, M. Rahimian, R. Attarnejad, Tsunami generation and associated waves in the water column and seabed due to an asymmetric earthquake motion within an anisotropic substratum, J. Geophys. Res. Oceans 121 (10) (2016) 7701–7715.
[33] A. Abdolali, J.T. Kirby, Role of compressibility on tsunami propagation, J. Geophys. Res. Oceans 122 (12) (2017) 9780–9794.
[34] T. Baba, S. Allgeyer, J. Hossen, P.R. Cummins, H. Tsushima, K. Imai, K. Yamashita, T. Kato, Accurate numerical simulation of the far-field tsunami caused by the 2011 Tohoku earthquake, including the effects of Boussinesq dispersion, seawater density stratification, elastic loading, and gravitational potential change, Ocean Modell. 111 (2017) 46–54.
[35] A. Abdolali, U. Kadri, J.T. Kirby, Effect of water compressibility, sea-floor elasticity, and field gravitational potential on tsunami phase speed, Sci. Rep. 9 (1) (2019) 1–8.
[36] G. Hendin, M. Stiassnie, Tsunami and acoustic-gravity waves in water of constant depth, Phys. Fluids 25 (8) (2013) 086103.
[37] P. Sammarco, C. Cecioni, G. Bellotti, A. Abdolali, Depth-integrated equation for large-scale modelling of low-frequency hydroacoustic waves, J. Fluid Mech. 722 (2013) R6.
[38] C.C. Mei, U. Kadri, Sound signals of tsunamis from a slender fault, J. Fluid Mech. 836 (2018) 352–373.
[39] B. Williams, U. Kadri, A. Abdolali, Acoustic–gravity waves from multi-fault rupture, J. Fluid Mech. 915 (2021).
[40] R. Omira, R. Ramalho, J. Kim, P.J. González, U. Kadri, J. Miranda, F. Carrilho, M. Baptista, Global tonga tsunami explained by a fast-moving atmospheric source, Nature 609 (7928) (2022) 734–740.